

# Specific Conformational Dynamics and Expansion Underpin a Multi-Step Mechanism for Specific Binding of p27 with Cdk2/Cyclin A

Maksym Tsytlonok<sup>1,†</sup>, Katherina Hemmen<sup>2,3</sup>, George Hamilton<sup>4</sup>, Narendar Kolimi<sup>4</sup>, Suren Felekyan<sup>2</sup>, Claus A.M. Seidel<sup>2</sup>, Peter Tompa<sup>1,5</sup> and Hugo Sanabria<sup>2,4</sup>

- 1 VIB-VUB Center for Structural Biology (CSB), Vrije Universiteit Brussel, Brussels, Belgium
- 2 Lehrstuhl für Molekulare Physikalische Chemie, Heinrich-Heine-Universität, 40225, Düsseldorf, Germany
- 3 Rudolf Virchow Center for Experimental Biomedicine, University of Würzburg, 97078, Würzburg, Germany
- 4 Department of Physics and Astronomy, Clemson University, Clemson, SC, 29634, USA
- 5 Institute of Enzymology, Research Centre for Natural Sciences, Budapest, Hungary

Correspondence to Hugo Sanabria: Department of Physics and Astronomy, Clemson University, Clemson, SC, 29634, USA. hsanabr@clemson.edu

https://doi.org/10.1016/j.jmb.2020.02.010

Edited by Sichun Yang

#### **Abstract**

The protein p27, a prominent regulatory protein in eukaryotes and an intrinsically disordered protein (IDP), regulates cell division by causing cell cycle arrest when bound in ternary complex with cyclin-dependent kinase (Cdk2) and cyclins (e.g., Cdk2/Cyclin A). We present an integrative study of p27 and its binding to Cdk2/Cyclin A complex by performing single-molecule multiparameter fluorescence spectroscopy, stoppedflow experiments, and molecular dynamics simulations. Our results suggest that unbound p27 adopts a compact conformation and undergoes conformational dynamics across several orders of magnitude in time (nano-to milliseconds), reflecting a multi-step mechanism for binding Cdk2/Cyclin A. Mutagenesis studies reveal that the region D1 in p27 plays a significant role in mediating the association kinetics, undergoing conformational rearrangement upon initial binding. Additionally, FRET experiments indicate an expansion of p27 throughout binding. The detected local and long-range structural dynamics suggest that p27 exhibits a limited binding surface in the unbound form, and stochastic conformational changes in D1 facilitate initial binding to Cdk2/Cyclin A complex. Furthermore, the post-kinase inhibitory domain (post-KID) region of p27 exchanges between distinct conformational ensembles: an extended regime exhibiting worm-like chain behavior, and a compact ensemble, which may protect p27 against nonspecific interactions. In summary, the binding interaction involves three steps: (i) D1 initiates binding, (ii) p27 wraps around Cdk2/Cyclin A and D2 binds, and (iii) the fully-formed fuzzy ternary complex is formed concomitantly with an extension of the post-KID region. An understanding of how the IDP nature of p27 underpins its functional interactions with Cdk2/ Cyclin A provides insight into the complex binding mechanisms of IDPs and their regulatory mechanisms. © 2020 The Authors. Published by Elsevier Ltd. This is an open access article under the CC BY-NC-ND license (http:// creativecommons.org/licenses/by-nc-nd/4.0/).

#### Introduction

A significant fraction of the eukaryotic proteome is unable to adopt a proper fold autonomously. These proteins are called intrinsically disordered proteins (IDPs). In fact, *in silico* prediction estimates that 30–40% of eukaryotic protein sequences contain long disordered regions under physiological conditions [1], and, so far, more than 800 IDPs are available in the DisProt database [2]. It is now widely

recognized that both disordered and ordered segments contribute to the activity of the proteins [3] and that these disordered regions can adopt ordered configurations or maintain functional disorder when bound to ordered domains [4–8]. Further, investigations of IDPs have shown that they can switch between conformational ensembles while maintaining their dynamic, disordered nature [9–14]. This switching behavior can occur stochastically for isolated IDPs [12] or can be induced through binding

interactions [13] or post-translational modifications like phosphorylation [14].

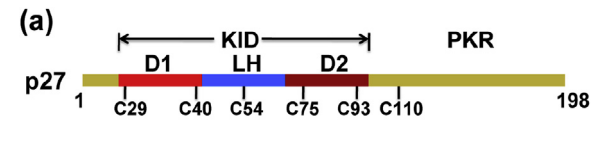
A prominent example of such a disordered-toordered transition upon binding is the multistep binding mechanism of p27 Kip1 (p27). p27 is a prototypical IDP that belongs to the Kip family of cyclin-dependent kinase inhibitor proteins. p27 regulates eukaryotic cell division by interacting with several cyclin-dependent kinase Cdk2/Cyclin complexes, phosphorylation, ubiquitination, and proteasomal degradation [15,16]. Mis-regulation of p27 function is significant in the progression of epithelial cancers, including those of colon, breast, prostate, lung, and ovary, as well as of brain tumors and lymphomas [17]. The crystal structure of the p27 kinase inhibitory domain (KID) in complex with Cdk2/ Cyclin A has provided insights into the mechanism by which p27 blocks the activity of the complex. p27 binds the Cdk2/Cyclin A complex by inserting Tyr88 of the KID domain into the ATP-binding pocket of Cdk2, thereby preventing catalytic activity [18]. This binding mode was among the first to be studied due to its functional importance and involvement in disease [19]. Regulation of p27 occurs via Tyr88phosphorylation by nonreceptor Tyr kinase (NRTK) Lyn and oncogene product BCR-ABL followed by intramolecular phosphorylation by Cdk2 at Thr187. Recently, we have proposed that bound p27 dynamically anticipates its phosphorylation through its intrinsic flexibility; hence, integrating various biological signaling inputs that result in altered Cdk2 activity, p27 stability, and, ultimately, cell cycle progression [20].

For investigating the mechanism of p27 binding with Cdk2/Cyclin A, we used single-molecule Förster Resonance Energy Transfer (smFRET) [21,22], single-molecule Fluorescence Anisotropy (smFA), stopped-flow kinetics studies, and replica-exchange discrete molecular dynamics simulations (rxDMD) [23]. Previously, we used a similar approach to identify distinct conformational states in a protein exhibiting fast dynamics by integrating smFRET and rxDMD [20]. Results of this study suggest that p27 undergoes a multi-step binding mechanism involving initial Cdk2/Cyclin A complex recognition by conformational selection followed by local induced folding in the binding region and further expansion to complete the ternary complex. Moreover, we find that the fully disordered region D1 in p27 serves as the guiding region for interaction with Cyclin A. In each step, the intrinsic flexibility in p27 dictates the interactions with the Cdk2/Cyclin A complex. This mechanism steers the interaction pathway toward a tightly bound inhibitory complex, with Cdk2/Cyclin A as the template for the final configuration of p27. In summary, the binding interaction involves three steps: (i) binding is initiated by domain 1 (D1), (ii) p27 wraps around Cdk2/Cyclin A by the binding of domain 2 (D2) and finally (iii) extension of the postKID region (PKR) to reach the fully-formed ternary complex.

#### Results

# Local flexibility of p27 reduced upon binding to Cdk2/Cyclin A

For detailing how the local structural dynamics of p27 are affected by interactions with the Cdk2/Cyclin A complex, we performed single-molecule fluorescence anisotropy (smFA) experiments with timecorrelated single-photon counting (TCSPC) data registration for the unbound p27. We compared them with recently published results for the bound form [20]. For these experiments, we labeled residues in and near the KID region of p27 with BODIPY-FL, namely sites C29, C40, C54, C75, and C93, mutated to cysteines (Fig. 1). Fluorescence emission from each single-molecule event was collected into parallel and perpendicular detector channels and used to calculate the average anisotropy per burst. The resulting distributions were quantified using photon distribution analysis (anisotropy PDA) [24,25]. smFA studies have been successfully employed to map protein mechanics



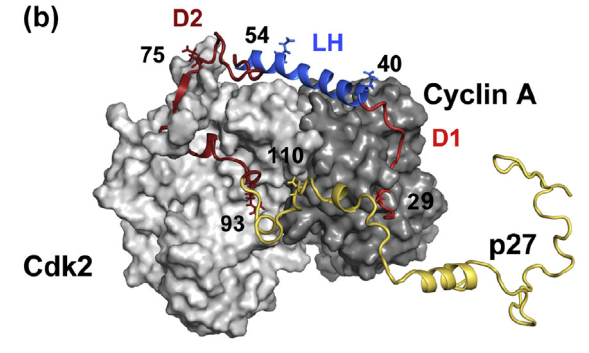


Fig. 1. Schematic representation of p27 and labeling sites, and cartoon representing p27 bound to Cdk2/Cyclin A. (a) Schematic diagram for p27 full-length protein. We show cysteine substitutions used for labeling along with the kinase inhibitory domain (KID). KID contains domain 1 (D1, light red), linker helix (LH, blue), domain 2 (D2, dark red). We refer to the remaining C-terminal residues as the post-KID region (PKR, dark yellow). (b) The interaction of p27KID with Cdk2/Cyclin A complex is shown based on the deposited crystal structure in the PDB (PDB: 1JSU) [18] and molecular dynamics simulations [59].

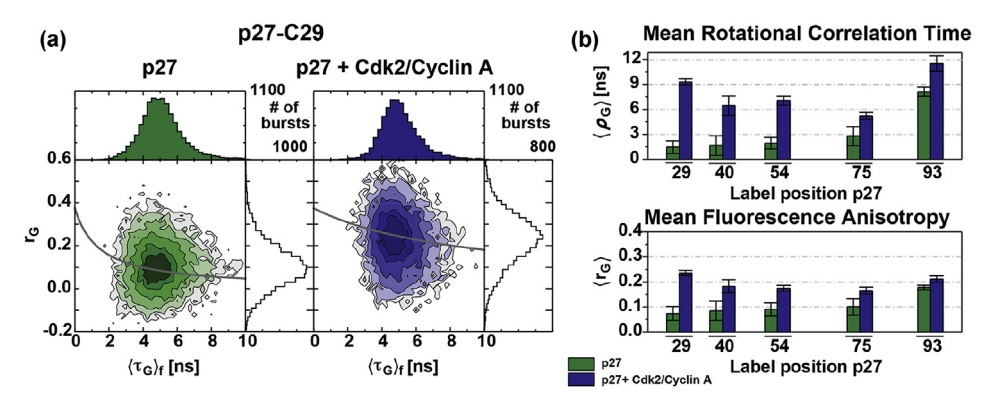


Fig. 2. Single-molecule fluorescence anisotropy reveals local dynamics. (a) Two-dimensional frequency histograms correlate the average fluorescence lifetime  $(\langle \tau_G \rangle_f)$  of the BODIPY label on the x-axis vs. scatter-corrected anisotropy  $(r_G)$  on the y-axis. We present one-dimensional frequency histograms along the axis and number of bursts at the right top corner. In grey are the Perrin equation (Eq. (10)) lines for the average rotational correlation time  $\langle \rho_G \rangle$ . There is a clear shift toward higher  $\langle r_G \rangle$  for bound p27 compared to the free form. (b) Both average anisotropy  $\langle r_G \rangle$  and rotational correlation time  $\langle \rho_G \rangle$  of p27 BODIPY-labeled samples increase when bound to Cdk2/Cyclin A (blue) compared to free p27 (green), indicating loss of flexibility throughout p27. Table S1 summarizes fit results and Fig. S1 shows the other variants.

Error bars represent the uncertainties as calculated by error propagation from Table S1, according to  $\sigma_x^2 = \sum_i \left(\frac{dx}{dy_i}\right)^2 \sigma_{y_i}^2$ .

and hydrodynamics in a benchmark study [26]. Fig. 2 summarizes the results of the experiments with p27.

For sites C29 and C40 in D1, apparent shifts were observed in the mean scatter-corrected fluorescence anisotropy  $(\langle r_G \rangle)$  to higher values in the bound p27 compared to the unbound protein. C54 in the LH region shows a similar increase in  $\langle r_G \rangle$ , albeit to a lesser extent. In each case, there was a definite shift in the  $r_G$  distribution, exemplified by that shown in the MFD histogram in Fig. 2a. For C75 and C93 in D2, the mean values of  $r_G$  showed little change and no apparent shift in the overall  $r_G$  distribution. These changes were also reflected in the mean rotational correlation times ( $\langle \rho_G \rangle$ ) of the samples (Fig. 2b, Fig. S1). PDA revealed two long-lived states with distinct anisotropies, high and low, respectively ( $r_G^H$ ,  $r_G^L$ ). Further, each free p27 sample exhibited a significantly higher fraction of the low anisotropy population compared to bound p27 (Table S1). The variants with labels in the p27KID region (C29, C40, C54) showed apparent increases in  $r_G^H$ , which do not occur for the samples with labels in or close to the PKR.

The profound changes in  $\langle \rho_G \rangle$ , calculated according to the Perrin equation (Eq. (10)), for the D1 and LH regions, in contrast to D2, indicate a distinct loss of local flexibility upon p27 binding with Cdk2/Cyclin A, suggesting the importance of these regions for recognition and binding of the complex. Further, anisotropy results show that p27 was free to sample high and low anisotropy states both when free and bound. However, binding resulted in a bias toward the high-anisotropy, low-flexibility states in the p27KID region. We conclude that rapid conforma-

tional sampling in the free form is essential for initial Cdk2/Cyclin A recognition and binding. At the same time, the high-anisotropy state is necessary for the binding interaction, becoming rotationally stabilized in the bound form.

#### Expansion of p27 upon binding to Cdk2/Cyclin A

For monitoring the overall conformation of p27 and its long-range dynamics, we used time-resolved, smFRET experiments (detailed in Methods). We engineered p27 variants with pairs of cysteine mutations at the residue pairs 29–54, 54–93, and 75–110 for FRET pair labeling [20]. These samples were labeled with Alexa 488 and Alexa 647 as donor and acceptor respectively, as previously reported [20]. These three FRET variants allowed us to probe the dynamics and relative distances of residues in the D1/LH (linker helix) (p27-C29-C54), LH/D2 (p27-C54-C93) and D2/PKR (p27-C75-C110), representing the different regions of interaction with the Cdk2/Cyclin A complex.

We monitored long-range dynamics by observing correlated changes of two FRET indicators of p27, the intensity-based FRET efficiency (E) versus the donor fluorescence-weighted average lifetime ( $\langle \tau_{D(A)} \rangle_f$ ). We performed experiments for FRET variants in the free form and compared them to the data that we had obtained previously for p27 bound to Cdk2/Cyclin A (Fig. 3). For example, p27-C29-C54 displayed a unimodal distribution at a high FRET efficiency with a maximum at E=0.85 and  $\langle \tau_{D(A)} \rangle_f=1.5$  ns in the free form. When bound to Cdk2/Cyclin A, the population peak shifted to a lower

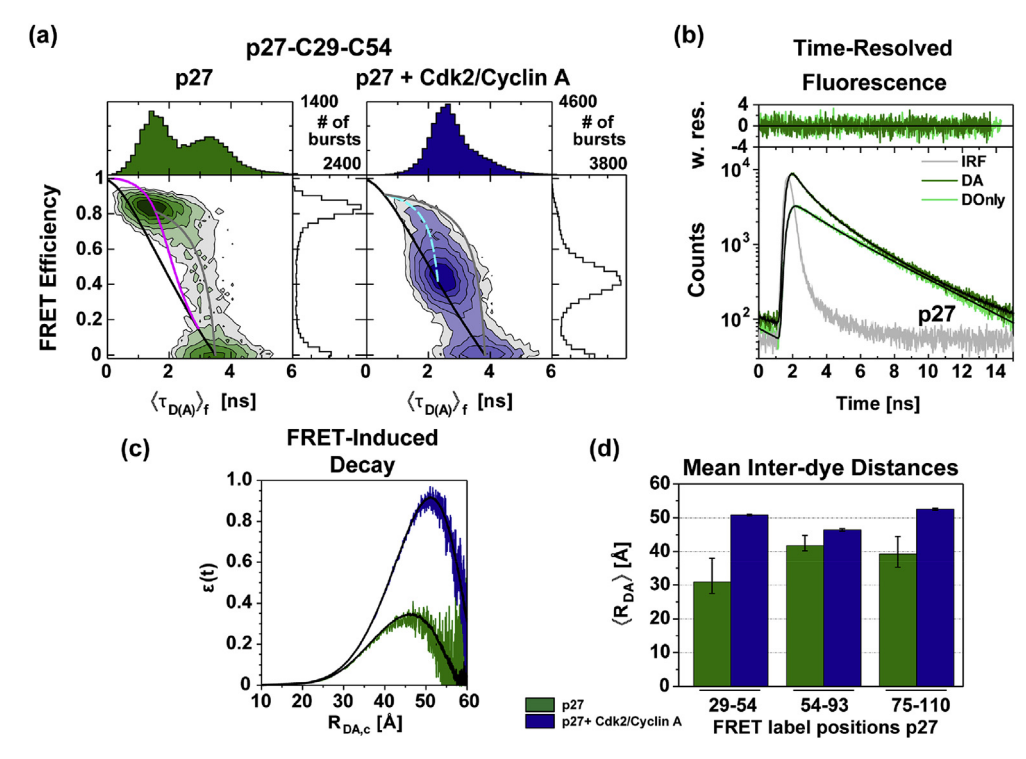


Fig. 3. Single-molecule Förster Resonance Energy Transfer reveals the expansion of p27 when bound to Cdk2/ Cyclin A. (a) The two-dimensional frequency histogram correlates the average fluorescence lifetime  $(\langle \tau_{D(A)} \rangle_f)$  with the FRET efficiency. The mean FRET efficiency for the sample p27-C29-C54 decreases significantly from the free to the bound form, indicating a longer inter-fluorophore distance. For each FRET indicator, we present the one-dimensional frequency histograms along the axes and number of bursts at the right top corner. Static FRET lines are in black. In grey, we display the bleaching line for both conditions. For the p27 alone, we added the dynamic WLC line in magenta, and for the Cdk2/Cyclin A bound to p27, the dynamic line as a dashed cyan line. (b) Time-resolved fluorescence decays for extracted DA (dark green), and DOnly populations (light green) from MFD histograms. The instrument response function (IRF) is shown in grey. Weighted residuals for the respective fit model (multi-exponential for DOnly (Eq. (9)), WLC for free p27) are shown on top. All bursts from the 2D histograms below E of ~0.18 were considered to belong to the DOnly population, i.e., either missing an active acceptor and too far D-A distances to allow for significant FRET to happen. Details are in Methods; Table S2 summarizes fit results. (c) FRET-induced donor decays as a function of critical distance,  $\epsilon(R_{DA})$ c), for seTCSPC analysis (Eqs. (7) and (8)). The black fit lines correspond to the WLC model for the free p27 and the two Gaussian states model for the p27 bound to Cdk2/Cyclin A. Raw data for free and bound p27 are shown in green and blue, respectively. We qualitatively compare the D-A distance with the highest probability from  $\epsilon(t)$  for the different double cysteine variants of p27 free and bound to Cdk2/Cyclin A. There is a clear shift toward longer  $R_{DA,c}$  for bound p27 compared to free p27. (d) The mean interdve distances and error bars calculated according to the WLC model for free p27 (Table 1) in green and according to data in previous work for the complex [20] in blue.

FRET efficiency at E=0.45 with  $\langle \tau_{D(A)} \rangle_f = 2.5$  ns (Fig. 3a). These changes in the FRET indicators indicate that, on average, the donor and acceptor are in closer proximity in the free form of p27 as compared to p27 bound to Cdk2/Cyclin A. A similar trend occurred in the two other FRET variants, p27-C54-C93 and p27-C75-C110, as shown in Fig. S2. It is worth noting that each of these samples contained a significant population of molecules with either donor label only or inactive acceptor, identified by  $E{\sim}0.0$  and  $\langle \tau_{D(A)} \rangle_f \sim 3.5-4.0$  ns.

To quantify the extension between the FRET labels, we used sub-ensemble time-correlated sin-

gle-photon counting (seTCSPC, see Methods). Here, we selectively analyzed the "DA" and "DOnly" (E< ~ 0.15) populations and constructed photon arrival time histograms. The fluorescence decays were fit with an interdye distance model that considers p27 as a Worm-Like-Chain (WLC, Eqs. (4)–(6)) in the free form (Fig. 3b) and we compared them with the recently reported population distance distributions for the complex form [20]. To best identify the mean interdye distance, we treated the FRET-induced (DA) donor fluorescence decay,  $\epsilon$ (t), via a model-free approach. We obtained  $\epsilon$ (R<sub>DA, C</sub>) as a function of the critical distance by a transformation

of the time axis to a critical distance axis, as detailed in Peulen et al. (2017) [27]. We found that the distribution peaked at 46 Å for the shown variant p27-C29-C54 (Fig. 3c). For the complex form, the peak shifted to 51 Å while the shape of the distribution was unchanged. In contrast, p27-C54-C93 showed both a shift of the maximum to higher distance and a reduction of tailing toward high FRET efficiency in the bound form. Bound p27-C75-C110 exhibited a similar shift again, but with an additional sharpening of the distribution. Thus, in all cases, complex formation led to a greater interdye distance, suggesting a general elongation of p27 molecules (Fig. S3).

For connecting the sub-ensemble representation of the WLC with the FRET efficiency distribution, we overlaid a FRET line on the MFD histograms using the relevant WLC parameters (Methods). This line (magenta) describes the polymeric characteristics of a WLC with a maximum extended length, L, and persistence length,  $l_p$  (Fig. 3a and Table 1). The WLC FRET line accurately captures the distribution of the FRET population in the MFD histogram for the free form. In contrast, the previously published dynamic FRET line (cyan) describes the dynamics in the ternary complex [20]. Additionally, we calculated the predicted mean interdye distance from the WLC model for each sample for later comparison to simulation (Table 1).

In summarizing the structural changes indicated by the FRET distributions and fitted models, we observed that for each labeled variant, the interdye distance increased significantly upon binding to the Cdk2/Cyclin A complex. In Fig. 3d, we compared the average mean interdye distance observed for all FRET variants in the free form using the WLC model and bound to the Cdk2/Cyclin A using a weighted average of the limiting states as previously determined [20]. Thus, we concluded that p27 acquires a more expanded configuration when in the ternary complex. Further, the WLC nature of free p27 allows the protein to sample a large ensemble of configurations spanning from compact to extended,

suggesting that p27 stochastic conformational changes are required for binding with Cdk2/Cyclin A through in the extended conformation. Additionally, the continuation of intrinsic p27 dynamics, although biased toward extended configurations upon binding, is compatible with a dynamic flycasting mechanism in the transition to a final, incomplex, induced configuration.

#### A dynamic binding to Cdk2/Cyclin A

The interdye distance distributions described above indicate a dynamic system that exchanges between an ensemble of local and long-range configurations on timescales that are faster than the observation times of individual molecules as determined by their diffusion properties. To further quantify the dynamics of p27 in its free form, including the diffusion time, we used filtered fluorescence correlation spectroscopy (fFCS) [28–31].

For fFCS, we deconvolved the observed fluorescence signal based on polarization- and spectrallyresolved fluorescence decays into component signals assigned to different fluorescence species. These sorted signals were, in turn, correlated with standard fluorescence fluctuation algorithms. By using a multiexponential relaxation model to characterize exchange processes between various populations at different FRET efficiencies (see Methods), we globally fit the species Auto- (sACF) and species Cross-Correlation functions (sCCF) with Egs. (11) and (12) for each FRET variant. Fig. 4 shows an exemplary set of correlation curves for the FRET variant p27-C29-C54 (other variants in Fig. S4). The fit model includes factors associated with structural fluctuations, diffusion parameters, and photophysical effects. The factor associated with structural fluctuations, and thus, changes in FRET efficiency, is given by a sum of four exponential decay terms.

Fig. 4b shows the timescales and amplitudes associated with these terms as a bar plot. We note that out of the four relaxation terms, only the fastest

**Table 1.** Interdye distances calculated from experiment and from AV simulations, as well as persistence lengths from the worm-like chain model. The maximal length is the fully extended polymer length for the worm-like chain model, reported with a 95% confidence interval.  $\kappa$  and  $l_P$  are reported for both fits of experimental data and AV simulations. There is general agreement between  $l_P$  from experiment and simulation, and those derived from simulation fit well within the confidence interval set by the experiment. Further,  $\langle R_{DA,Sim} \rangle$  calculated directly from AV simulations agree with  $\langle R_{DA,Exp} \rangle$  determined from the WLC model. All distances are expressed in angstroms (Å).

Sample/value	C29-C54	C54-C93	C75-C110
$\langle R_{DA,Exp} \rangle$ [Å]	30.9 (27.6–38.1)	41.8 (40.3–44.8)	39.3 (35.3–44.6)
$\langle R_{DA,Sim} \rangle [\mathring{A}]$	37.6	44.4	37.4
Max Length [Å]	73.8 (62.0—104.0) 0.39	56.1 (50.0—62.0) 1.02	67.7 (63.0–73.0) 0.60
$\kappa_{DA,Exp} \ \kappa_{DA,Sim}$	0.50	1.00	0.56
$l_{P,Exp}$ [Å] $l_{P,Sim}$ [Å]	29.0 (19.0-47.0)	57.0 (42.0-94.0)	41.4 (36.0-49.0)
$l_{P,Sim}[ extsf{A}]$	37.0	56.1	37.8

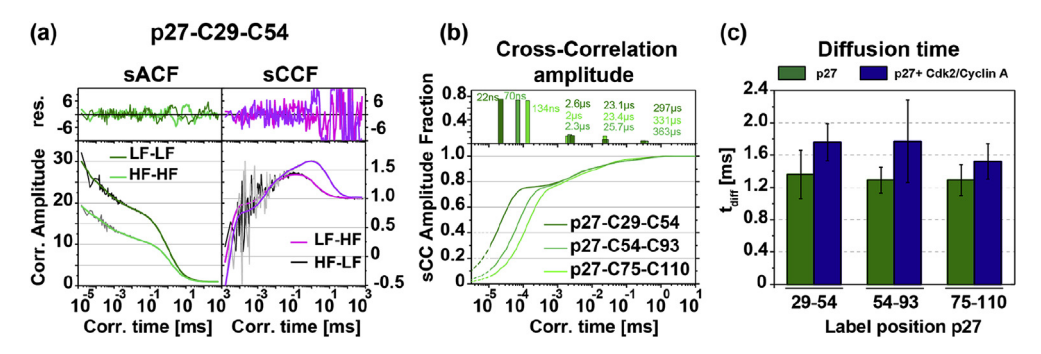


Fig. 4. Filtered fluorescence correlation spectroscopy reveals sub-millisecond conformational dynamics. (a) Filtered FCS auto (left) and cross (right) correlations. Residuals of the fits for species-specific auto (sACF) and cross-correlation functions (sCCF) are shown at the top of each correlation curve. Global fitting allowed internally consistent identification of timescales of conformational dynamics and photophysical effects. (b) Extracted anticorrelation terms for the p27-C29-C54, p27-C54-C93, and p27-C75-C110 variants free in solution. Bar plot for population fractions vs. correlation time is shown at the top. p27-C29-C54 exhibits the fastest dynamics in the timescale typical of fast chain dynamics. (c) Characteristic diffusion time for p27 free and bound to Cdk2/Cyclin A was determined by fFCS. The diffusion time is faster for the free form (green) in all double cysteine variants compared to the bound form (blue). Table S3 summarizes all fFCS fit parameters.

terms exhibit significant differences between the FRET variants. In contrast, the amplitudes of the respective relaxation terms are very similar among the variants. In particular, we observe that the fastest term corresponded to the FRET variant p27-C29-C54, followed by the p27-C54-C93, and lastly, p27-C75-C110. Because these FRET pairs indicated the timescales of dynamics observed in the regions D1/LH, LH/D2, and D2/PKR respectively, we can conclude that fast exchanges occurring in D1 are critical in guiding the expansion of p27. In contrast, the PKR dynamics would serve as the rate-limiting step in the overall opening.

As part of the fFCS analysis, we also obtained the characteristic diffusion time  $t_{\rm diff}$  that can be related to the hydrodynamic radius of p27 free and in complex using the Stokes-Einstein relationship (Table S3, S4). A comparison of  $t_{\rm diff}$  for each sample corroborated our findings from smFRET and seTCSPC data that p27 expands from its free form to the complex form (Fig. 4c and Table S3).

# Weak interactions guiding p27KID binding with Cyclin A

Next, to understand the mechanistic details of the transition between unfolded and bound, expanded conformations of p27KID, we performed a series of rapid-mixing experiments with truncated p27KID (Fig. 1). Intrinsic tryptophan fluorescence in Cyclin A (W217, W372), Cdk2 (W167, W187, W227, W243), and p27KID (W60, W76) allowed direct monitoring of the kinetics of binding. Upon p27KID binding to Cyclin A, we detected both a very fast and a slow phase associated with a decrease and an

increase in fluorescence, respectively (Fig. S5). For p27KID binding, fluorescence kinetics could be adequately fitted by two exponentials at 25 °C. The dependence of the observed fast rate on p27KID concentration is linear, whereas the slow rate is independent of p27KID concentration (Fig. 5a, dark grey lines correspond to increasing concentrations of p27; yellow line for experiments at increasing concentration of Cyclin A). These data suggest that after the initial fast binding reaction of p27KID with Cyclin A, one of the proteins undergoes slower structural rearrangements associated with less quenching of the tryptophan fluorescence. The slope of the linear fit gives the association rate constant of the reaction ( $\bar{k}_{on} = 5 \times 10^7 \, M^{-1} s^{-1}$ ), and the intercept of the line with the Y-axis gives the dissociation rate constant (koff). Here, the intercept with the x-axis is close to 0, and therefore, it was not possible to determine the off-rate precisely. We measured kinetic traces of p27KID with Cdk2 at a range of protein concentrations in 5× excess of p27KID or Cdk2. In these experiments, the binding kinetics followed a mono-exponential increase in fluorescence, and a linear regression model was used to fit the rate constants (Fig. 5a and b and Fig. S5). The  $k_{on}$  of this reaction was very slow (1  $\times$  10<sup>-2</sup> M<sup>-1</sup>s<sup>-1</sup>), in agreement with previous surface plasmon resonance results [19].

In further kinetic experiments, we measured the intrinsic tryptophan fluorescence during the binding reaction of p27KID with Cdk2/Cyclin A complex (Fig. 5c and d). As observed with Cyclin A alone, the kinetic traces again exhibited a rapid decrease in fluorescence followed by a slower increase, although with a relatively smaller amplitude

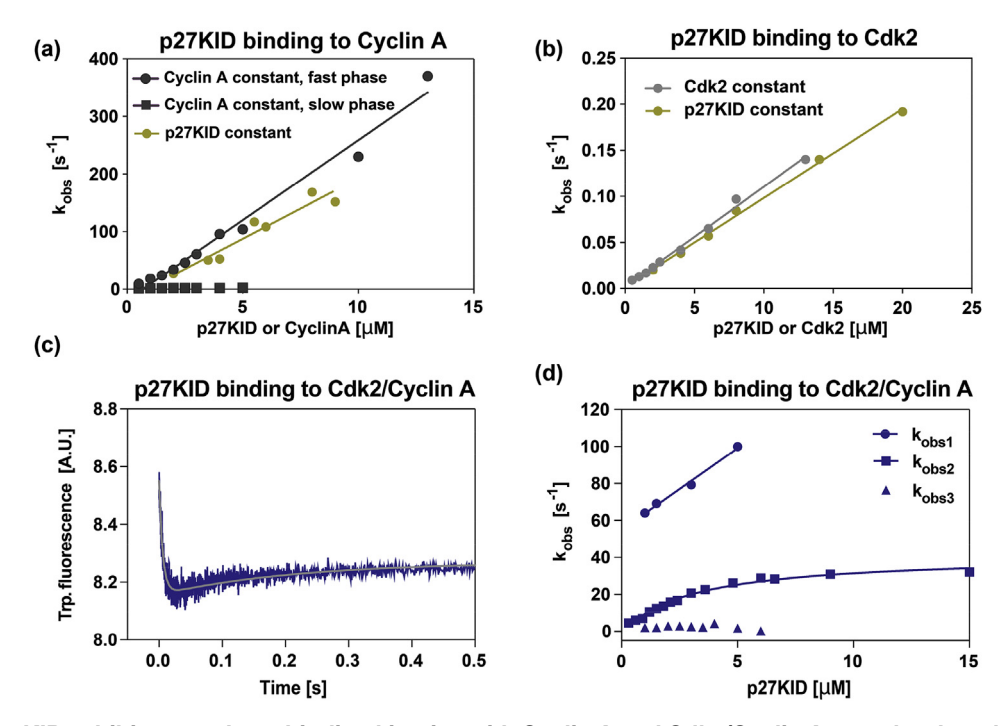


Fig. 5. p27KID exhibits two-phase binding kinetics with Cyclin A and Cdk2/Cyclin A complex, but slower overall interaction kinetics with Cdk2 as observed by tryptophan fluorescence. (a) Binding interaction of p27KID with Cyclin A exhibits a fast phase with a linear dependence on p27KID concentration ( $k_{on} = 5 \times 10^7 \, M^{-1} s^{-1}$ ) and a slow phase that is independent of p27KID concentration, suggesting that initial recognition is followed by conformational rearrangement in one of the two proteins. The binding interaction at constant p27KID concentration exhibits linear dependence on the concentration of Cyclin A. (b) Observed rate constants for the interaction of p27KID with Cdk2 shows only a monoexponential increase with Cdk2 or p27KID concentration at constant p27KID or Cdk2, respectively, and overall slower kinetics ( $k_{on} = 1 \times 10^{-2} \, M^{-1} s^{-1}$ ) than p27KID with Cyclin A or complex. Constant concentration conditions for Cdk2 or p27KID were maintained at  $5 \times m$  molar excess of p2KID and Cdk2, respectively. (c) The kinetic trace of full-length p27 (3.5  $\mu$ M) mixed with Cyclin A (3.5  $\mu$ M) shows a rapid decrease followed by a slow increase in the tryptophan fluorescence. At long times, the fluorescence levels off. (d) The kinetics for the interaction of p27KID with Cdk2/Cyclin A complex. The rate constant  $k_{obs1}$  is fast, linearly dependent on the concentration of p27, and similar to the rate observed in interaction with Cyclin A.  $k_{obs2}$  saturates at high concentration of p27KID with a hyperbolic dependence. In contrast,  $k_{obs3}$  has a very low, concentration-independent phase. We have summarized these data in Table S5.

(Fig. 5c). Linear regression of the observed fast initial phase resulted in an apparent  $k_{on1} = 3.5 \times 10$ -M<sup>-1</sup>s<sup>-1</sup>, which is very similar to the value observed for the Cyclin A binding reaction. However, this time we obtained  $k_{off1} = 26 \text{ s}^{-1}$ . Interestingly, the k<sub>obs2</sub> saturated at higher p27KID concentrations and the rate constants as a function of protein concentration fit to a hyperbolic binding model with  $K_{d1} = 7 \,\mu\text{M} \pm 3 \,\mu\text{M}$  and  $k_{off1} + k_{off2} = 32 \,\text{s}^{-1}$  (Fig. 5d). The  $K_{d1}$  obtained from the hyperbolic fit was like the  $K_{d1}$  obtained from apparent  $k_{off1}$  and  $k_{on1}$  ( $k_{off1}$ /  $k_{on1} = 0.7 \mu M$ ). The slowest phase,  $k_{obs3}$ , was concentration-independent and was challenging to measure due to its small amplitude; it most likely corresponds to the slowest phase also observed in the Cyclin A/p27KID binding reaction. The curvature of the second binding reaction (k<sub>obs2</sub>, Fig. 5d) implies that the accompanying Cdk2 is essential for the conformational transition concomitant with the binding of p27KID with Cdk2, in agreement with the previously published induced-fit mechanism [19]. The overall  $K_{\rm d}$  of p27KID with Cyclin A is 20 nM [19], and our new data suggest that the initial binding step leads to the formation of a weak encounter complex (~1–10  $\mu M)$  with high dissociation rate constant. Further conformational rearrangements in p27KID and folding of some residues upon binding contribute to the stronger binding of nM affinity.

# Long-range conformational rearrangements in p27 upon binding to Cyclin A

Since both p27 and Cyclin A contain tryptophan residues, we used designed cysteine variants of p27, which accommodate fluorescent dyes at specific locations in the amino acid sequence. We used the single cysteine variants with the fluorescent dyes Alexa 488 (charged) at positions C93 and C75

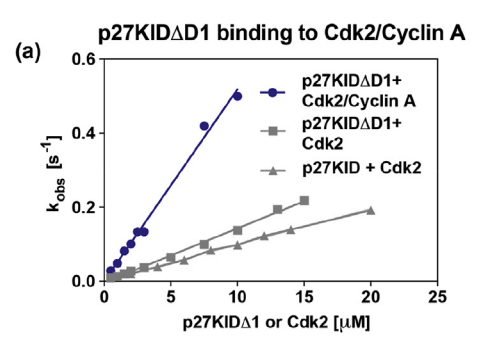
and BODIPY-FL (hydrophobic) at positions C29 and C54. First, we measured the association reaction of p27 with Cyclin A, followed by dye fluorescence at >530 nm (Fig. S6). The on-rates observed are very similar to the ones previously measured by tryptophan fluorescence, suggesting that labeling with the dye does not significantly affect the binding mechanism (Table S5, Figure S7). Interestingly, although the dyes at positions C54, C75, and C93 were not in the proximity of the Cyclin A interaction site in D1, all the kinetic reactions displayed significant changes in fluorescence upon binding. The C54 data set displayed an increase, rather than a decrease, in fluorescence, pointing to a difference in structural rearrangements in the LH to D1 and D2 regions in p27 (Fig. S6). These data suggest that long-range allostery is present in the binding reaction of p27 D1 and LH with Cyclin A in the regions of p27 away from the binding site and folding of the linker helix at least partially occurs in the interaction with Cyclin A.

# D1 in p27 is the leading recognition site for binding initiation

We performed the mutagenesis of p27 and analyzed the fast binding kinetics with Cyclin A by tryptophan fluorescence, to define the first interaction site in the binding reaction,. The mutants located in D1 (e.g., A28G, C29A, E39A) and LH (E40A, A55G, M52A) did not have a significant effect on the first very fast or the second, slow rate constants (Fig. S7). Therefore, we designed a truncated variant of p27 lacking D1 (p27KID $\Delta$ D1) and measured its association kinetics with Cyclin A and Cdk2 alone and with Cdk2/Cyclin A complex (Fig. 6). The association kinetics of p27KIDDD1 with Cyclin A alone did not give any fluorescence change, indicating that the binding did not occur. The binding reaction of p27KID∆D1 with Cdk2 showed a rapid increase in tryptophan fluorescence and the concentration dependence of rate constants on protein concentration resulted in a linear behavior with 1.5 times increase in the  $k_{on1}$  (1.5 × 10<sup>-2</sup> M<sup>-1</sup>s<sup>-1</sup>) rate in comparison to the  $k_{on1} = 1 \times 10^{-2} \text{ M}^{-1} \text{s}^{-1}$  of p27KID with Cdk2 (Fig. 6a). When we monitor the binding of p27KIDΔD1 with Cdk2/Cyclin A, the fluorescence increase was mono-exponential, although the kon rate was now five times faster  $(5 \times 10^{-2} \text{ M}^{-1} \text{s}^{-1})$  than the  $k_{on}$  for Cdk2/p27KID interaction. The very fast phase was again not present. In further experiments, we followed the association of p27KID with the Cdk2/Cvclin A/ p27KIDΔD1 preformed complex. Again, we monitor the binding by tryptophan fluorescence and fit the binding traces with two exponentials with a very fast and a slow phase. The very fast phase showed a linear dependence on protein concentration with the  $k_{on}$  of  $1.6 \times 10^7$  M<sup>-1</sup>s<sup>-1</sup>, whereas the slow phase was concentration-independent (Fig. 6b). These data indicate that D1 interaction with Cyclin A is the main driving force in the association kinetics, and LH contributes only marginally to the interaction with Cyclin A and the Cdk2/Cyclin A complex.

# Simulations exhibit conformational dynamics of LH and PKR in free p27

For bridging the smFA, smFRET, fFCS, and binding kinetics experiments of free p27 through independent validation, we performed Replica-Exchange Discrete Molecular Dynamics (rxDMD) [23] simulations for the full-length p27, totaling 1  $\mu$ s of simulation time (Fig. 7a; Methods). The radius of gyration, R<sub>g</sub>, was calculated as a measure of compactness throughout the trajectory (Fig. 7b). Qualitatively, p27 rapidly exchanges between at least two state ensembles with distinct R<sub>g</sub> (Fig. 7c). Fits to Gaussian-distributed states suggested a 3-ensembles model (Fig. 7d) with population means R<sub>g</sub> of 2.4 nm, 3.0 nm, and 4.4 nm, respectively



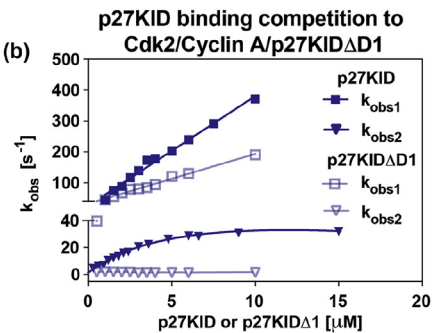


Fig. 6. Truncation of p27KID to exclude D1 slows initial binding to Cyclin A and Cdk2/Cyclin A. (a) The fast interaction phase of p27KID $\Delta$ D1 with Cdk2/Cyclin A complex and Cdk2 shows 5-fold ( $k_{obs} = 5.0 \times 10^{-2} \, M^{-1} s^{-1}$ ) and 1.5-fold ( $k_{obs} = 1.5 \times 10^{-2} \, M^{-1} s^{-1}$ ) increase in  $k_{obs}$ , respectively, over the interaction of p27KID with Cdk2 ( $k_{obs} = 1.0 \times 10^{-2} \, M^{-1} s^{-1}$ ). (b) The association kinetics for the interaction of p27KID with preformed Cdk2/Cyclin A/p27KID $\Delta$ D1 complex. The binding traces show two exponential decays with a very fast and a slow phase like experiments with p27KID (Fig. 5).

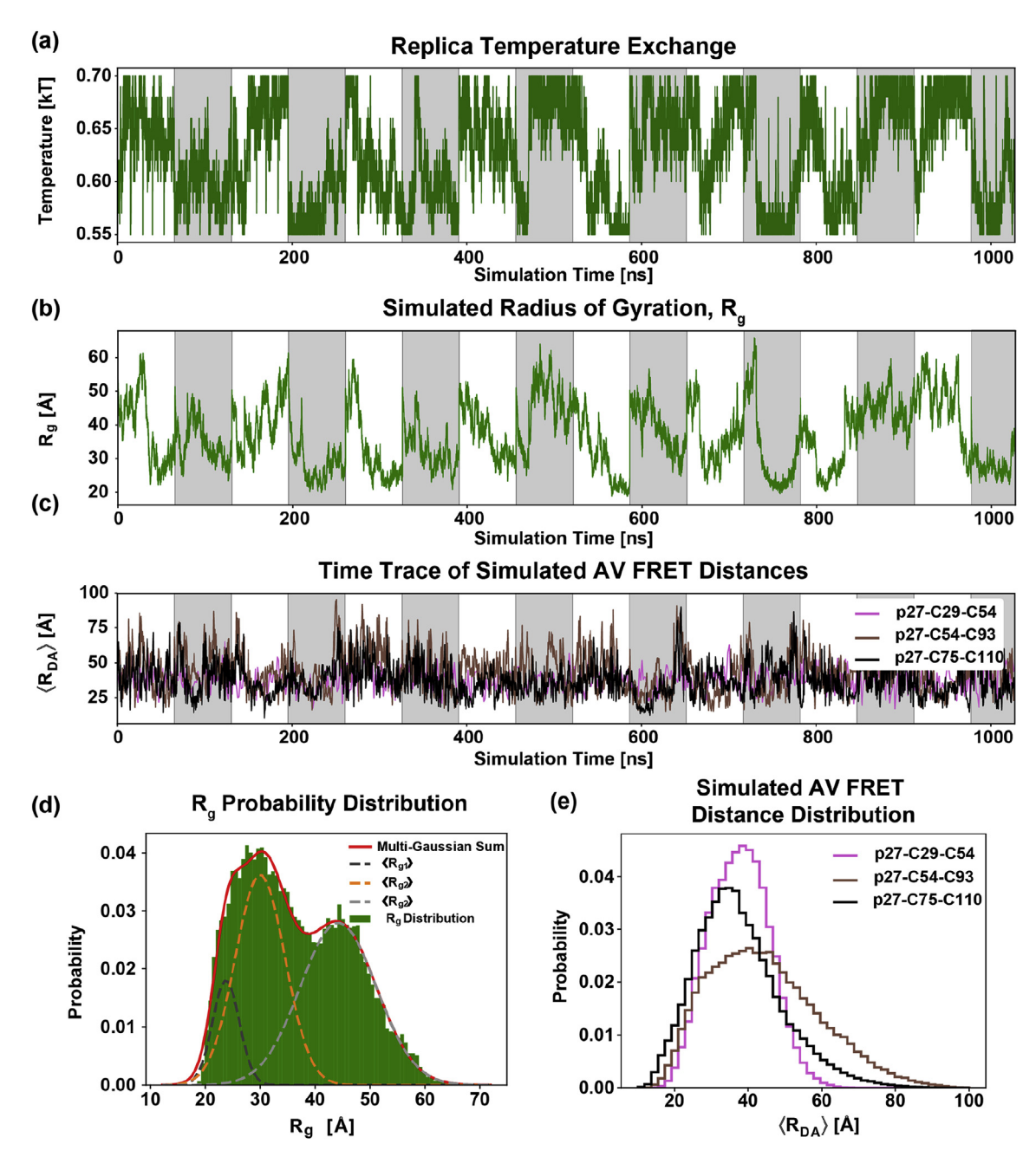


Fig. 7. p27 simulations show rapid changes in the degree of compactness through  $R_g$ . (a) Time traces for simulation bath temperature. Alternating grey and white vertical bars indicate different simulation replicas in 16 temperature baths from 275 K to 350 K. (b-c)  $R_g$  and  $\langle R_{DA} \rangle$  traces indicate fast changes in conformation, mirroring FRET experiments. (d)  $R_g$  distribution from simulations, fitted to a three Gaussian-distributed state model (solid red). Individual Gaussians, with means  $23.8 \pm 0.3$  Å,  $30.0 \pm 0.6$  Å, and  $44.2 \pm 0.5$  Å, respectively, are shown as dotted curves. Three Gaussians were chosen based on improvement in confidence given by the F-test when compared to one or two-Gaussian models. Fits were performed with the optimize.curve\_fit algorithm from the SciPy Python package [60], and uncertainties were computed as the square roots of the diagonals of the output covariance matrix. (e) AV-derived FRET distance distributions for comparison to experiment. Table 1 summarizes the calculated mean interdye distances and persistence lengths for each FRET variant calculated from simulated and experimental data. The relative persistence lengths calculated from simulated and experimental data are in general agreement.

(Table S6). To estimate the diffusion characteristics of p27, we calculated the ratio of  $R_{\rm g}$  and  $R_{\rm h}.$   $R_{\rm h},$  in the biophysical sense, is calculated as the Stokes radius under the assumption of hard sphere-like diffusion, while  $R_{\rm g}$  tells us about the overall compactness of the molecule. Thus, the ratio  $R_{\rm g}/R_{\rm h}$ 

provides shape information indicating how the diffusive properties of a molecule deviate from the compact hard-sphere model [32]. The mean  $R_g$  was calculated directly from simulation, as opposed to the typical methods like SAXS, giving 36.28 Å. The  $R_h$  determined from FCS data is 17.9 Å (Table S4).

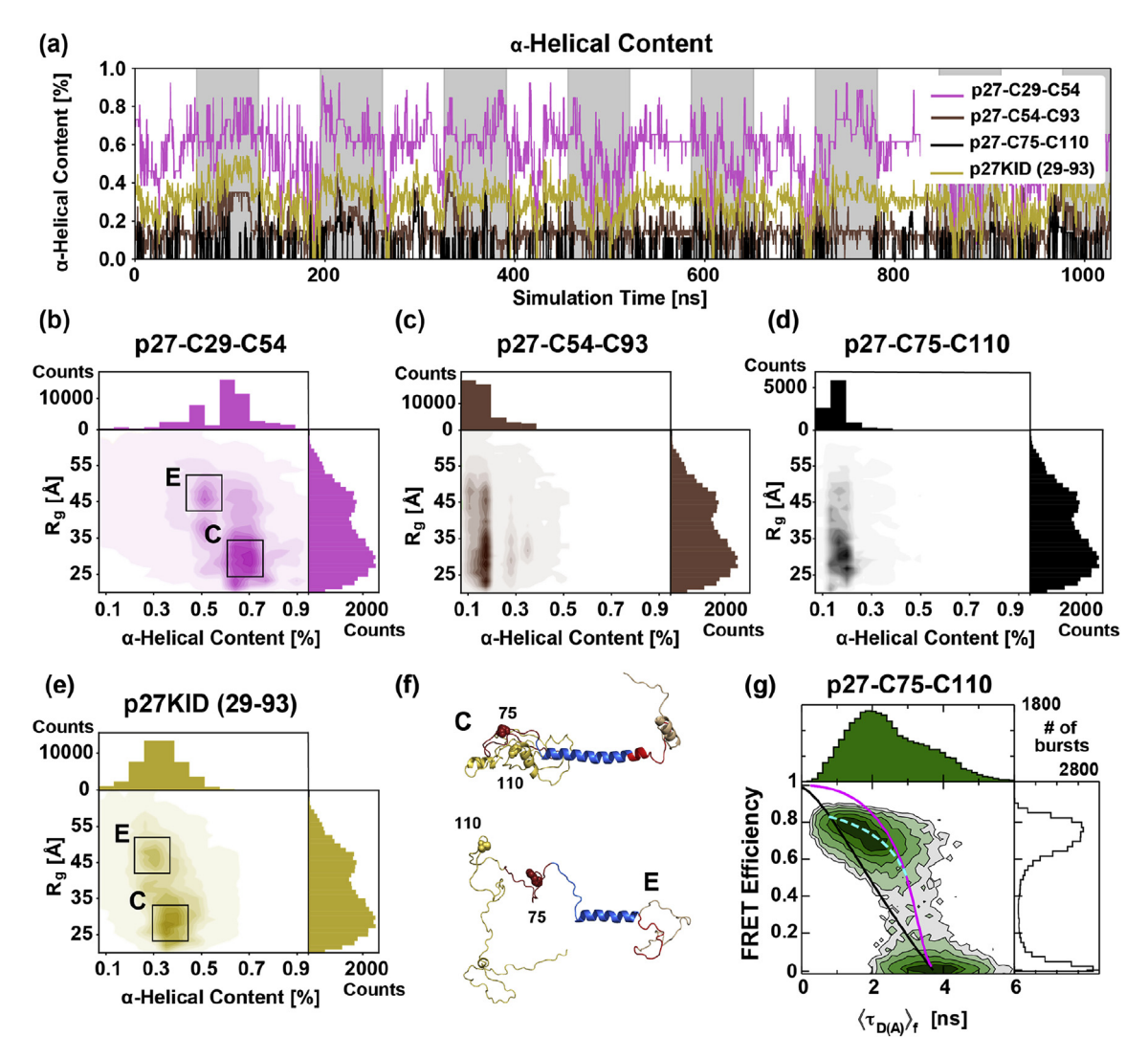


Fig. 8. Free p27 simulations exhibit conformational ensemble switching and nascent α-helical structure formation. (a) Time trace of α-helical content for the three protein sections encompassed by the FRET labeling sites, as well as for the full p27KID region. The C29–C54 range has the highest helical content throughout the trajectories, but all ranges exhibit rapid switching between high and low α-helical content. (b-e) Contour plots showing  $R_g$  and α-helical content in each region for each frame of the simulation. p27-C29-C54 accounts for most of the maintained α-helical content, while both p27-C29-C54 and p27-C54-C93 exhibit large overall changes in α-helical content. (f) Representative structures from simulation representing the trends seen in (b) and (e). "E" corresponds to the extended, higher  $R_g$  peak in the distribution with lower α-helical content in both (b) and (e) while "C" represents the more compact state. Structures were identified by screening the trajectory from basins indicated in (b) and (e) simultaneously. They are aligned along the short segment of α-helical LH in "E". (g) Experimental MFD plot for free p27-C75-C110. Here we have fitted the static and dynamic FRET lines (black and cyan, respectively; see Methods), as well as the dynamic WLC model line (magenta). The cyan dynamic FRET line is calculated for two Gaussian-distributed states, one corresponding to the bound-like conformation observed in FRET experiments for p27 in complex with Cdk2/Cyclin A, and the other the fully-extended limit of the WLC model. Input parameters for FRET lines can be found in Table S2a for the static line and Table S2b for the WLC. We observe the transition between dynamic ensembles in the compaction and elongation of the PKR.

The ratio  $R_o/R_h = 2.03$  indicates that the free p27 has an average diffusion behavior deviating quite far from the compact sphere model; hence, behaving like a more elongated shape like a prolate ellipsoid [32]. The elongated shape is consistent with the behavior observed in the Movie S1, showing switching between extended and compact configurations and, even in the compact structures, the LH helix extending from the compact post-KID region. Additionally, in silico interdye distances were calculated via Accessible Volume (AV) simulations (Fig. 7c and e: see Methods) [33,34] for each simulated structure and used to calculate the effective persistence lengths between the labeling sites for direct comparison with experimental persistence lengths according to the worm-like chain model (Fig. 3, Fig. S2 and Table 1). Both regions C29-C54 and C75-C110 exhibited relatively short persistence lengths (/- $_{\rm P,DA,Sim,29-54}=37.0$  Å,  $I_{\rm P,DA,Sim,75-110}=37.8$  Å) while the region 54–93 exhibited a longer persistence length ( $I_{P,DA,Sim,54-93} = 56.1$  Å). Further, there is a general agreement between the mean interdye distances calculated for experiments and simulations according to the worm-like chain model. Moreover, the simulation displayed that the PKR of p27 undergoes a slow elongation and contraction process characterized by residues "bunching" near the LH (Movie S1). Such secondary structure reorganization may be crucial in changing the accessibility of binding sites in the helix for interaction with the Cdk2/ Cyclin A complex or other binding partners and provide a possible explanation for timescales in the 100s of us observed by fFCS experiments.

Supplementary video related to this article can be found at https://doi.org/10.1016/j.jmb.2020.02.010.

To probe the role of secondary structural flexibility in the structural dynamics of free p27, we processed the rxDMD simulation trajectories using secondary STRuctural IDEntification (STRIDE) [35]. The STRIDE algorithm assigns secondary structures to a file of protein atomic coordinates through consideration of hydrogen bond energy and backbone geometric information based on comparison to protein structures deposited in the PDB. It has been hypothesized that binding to the Cdk2/Cyclin A stabilized the LH of p27KID following the foldingupon-binding mechanism [36], but is unstable in the free form, and thus, undergoes rapid folding and unfolding (Fig. 8a). Thus, the percentage helical contents of p27 regions were plotted with Rg to identify the subpopulations differentiated by helical structure formation and p27 compaction (Fig. 8b-e). Across the entire KID region and between the residue pair C29-C54 used for FRET labeling sites (the region containing the LH), we identified subpopulations by correlating the percentage helical

content with  $R_g$  (Fig. 8b and e). Changes in  $R_g$  were primarily due to changes in the compactness of the PKR, leading to two distinguishable ensembles, one extended and one compact.

Further, the LH appears conserved in a nascent sense, with the total helical content varying except in a small region where the LH helix was conserved. In Fig. 8f, we display representative structures, visualized using VMD [37], for the two major basins. Such unfolding and refolding of the helical region may be necessary for target recognition in binding to Cdk2/Cyclin A, compatible with conformational selection and induced-fit mechanisms.

Further, for the p27-C75-C110 variant, we observe switching between conformational ensembles with extended and compact PKR (Fig. 8g). The dynamic FRET line (cyan) connects a Gaussian distributed state intersecting the static FRET line (black line Fig. 8g) with the FRET line of the WLC model (magenta line). We conclude that the compact ensemble may protect against post-translational modification and nonspecific interactions of p27 before global extension occurs in the bound form.

#### **Discussion and Conclusions**

Global expansion in p27 upon binding: a compact state as a protection against proteolysis and nonspecific interactions

Cyclin A displays a short recognition element for 12 residues of disordered D1 in p27 that is also able to recognize multiple targets with different structures. Here, we report that D1 is crucial in initiating the binding reaction and facilitating short- and longdistance conformational rearrangements in p27, leading to folding of specific segments in p27 for binding to the Cdk2/Cyclin A complex. It is not a coincidence that the recognition motif lies in the fully disordered D1 of p27 and does not acquire any structural elements upon binding to Cyclin A [18]. The fluctuating ensemble of conformations in this segment even persists in the bound form as a fuzzy complex [8,20,38]. The structural disorder in D1 presents many advantages to the functionality of p27, such as specificity without excessive binding strength and the ability to fulfill more than one function by binding to different cyclin proteins, socalled moonlighting [39]. However, p27 contains residual  $\alpha$ -helical structure in its free form [40], offering some protection from proteolytic degradation by shielding specific segments and exposing others. smFRET data and rxDMD simulations show that p27 samples a mostly compact structural ensemble in its free form, rather than the conformation with fully opened-stretched D1-D2 regions and PKR as in the bound form, providing a limited binding surface and preventing p27 from having multiple contact points on the target proteins Cdk2 and Cyclin A at the same time. Therefore, it is not surprising that the  $k_{\text{on}}$  rates of p27KID with Cdk2 and Cyclin A differ by many orders of magnitude, although the  $K_{\rm d}$  values are very similar. The compact configurational ensemble in p27 may regulate the interaction pathway with the preferred regions in the IDP.

Our data demonstrate that a long IDP can interact with its binding partner by combining conformational selection and induced-fit mechanisms. Binding of IDPs is generally characterized by high specificity to multiple partners, as is the case for p27. IDPs are frequently involved in signal transduction and cell-cycle regulation, gene expression, and chaperone action [4,41] in which high  $k_{on}$  and  $k_{off}$  rates would be beneficial. However, many IDP-protein interactions have sub- $\mu$ M affinities. The stabilization of these interactions is usually accompanied by the formation of transient structural elements, as it is the case for p27. However, the newly acquired single-molecule fluorescence data indicate that not all of the

segments are immediately accessible, likely shielding p27 from unspecific interactions. The exposure of D1 may lead to binding recognition and serves as the primary contact point with Cyclin A. Moreover, the segmental nature of D1 increases the association rate by anchoring only a few amino acids and forming an encounter complex, which facilitates further interactions with the complex through progressive elongation. Interestingly, both electrostatic and hydrophobic amino acids steer the interaction of D1 of p27 with the Cyclin A protein.

# Multistep mechanism of p27 binding with Cdk2/ Cyclin A

The p27 protein can interact with more than one partner, and it also connects two globular proteins, Cdks, and cyclins, via a linker helix (LH) that imparts structural variability depending on the type of interacting partner, similar to p21 [42]. Therefore, the most plausible mechanism to explain the binding of p27 to Cdk2/Cyclin A complexes engages the combination of several previously described models. First, from the ensemble of p27 conformations, conformational selection takes place in initial binding

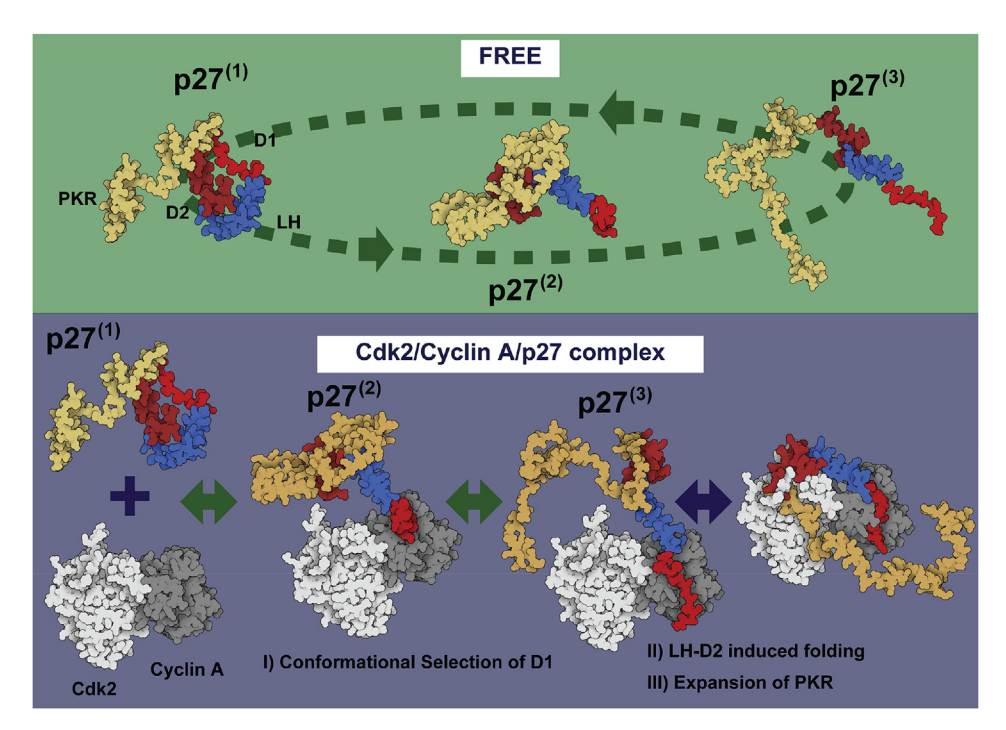


**Fig. 9.** Cartoon models for the conformational dynamics of free p27 and the multi-step binding interaction with Cdk2/Cyclin A. p27 stochastically samples numerous conformations in the unbound form. Nevertheless, we observed dynamic transitions between distinct compact and extended ensembles for unbound p27 via FRET and DMD simulations (green). Numbering corresponds to the ordering of conformational changes during the binding interaction of p27 with Cdk2/Cyclin A complex. I) Conformational selection of D1 to initiate binding corresponds to the transition from p27<sup>(1)</sup>, basin C from Fig. 8f, to p27<sup>(2)</sup>. II) Induced-folding of LH to facilitate binding of D2 to Cdk2 occurs next. p27<sup>(3)</sup> with folded LH and extended PKR corresponds with basin E in Fig. 8f. III) Expansion of the PKR following binding of D2 results in the final, fuzzy ternary complex. Cartoon models were generated using Illustrate [61].

to Cdk2/Cyclin A (Fig. 9, transition from p27<sup>(1)</sup> to p27<sup>(2)</sup>) by exposing D1. Next, the local induced folding mechanism happens through structural adaptability of the LH in p27 and the binding of D2 to Cdk2 (p27<sup>(3)</sup>). Finally, extension, characterized by extension of the PKR wrapped near the Cdk2, allows for additional interactions of the p27 with other molecules while bound in the fuzzy complex (Fig. 9).

In line with our results, previous studies have reported that the unbound form of p27KID behaves with IDP characteristics for D1 and D2. Further, the LH region exhibits nascent helical conformation [43-46], such as that observed in rxDMD simulations performed in this study. Also, circular dichroism studies [40,46,47] and isothermal titration calorimetry [47] confirmed the disordered conformation for p27KID in solution. While we do not observe the formation of significant secondary structure in the PKR, rxDMD simulations and FRET variant p27-C75-C110 corroborate switching between conformational ensembles in which the PKR is either generally extended, acting like a worm-like chain, or compact. This switching may protect free p27 from nonspecific interactions and post-translational modifications, which lead to degradation while also providing the necessary flexibility to expose phosphorylation sites in the bound form. Other IDPs have been observed to exhibit ensemble switching concomitant with post-translational modifications like phosphorylation [9-13]. Our findings suggest that the dynamics of many IDPs may play a key role in their biological functions.

The complexity of the interaction opens the opportunity for a variety of regulation events in response to cellular signals. For example, fluctuations in D2 allow Y88 to be phosphorylated by NRTK to reactivate the Cdk2/Cyclin A complex. Furthermore, this phosphorylation event induces long-range conformational rearrangements and shifts the equilibrium from bound D1 to an unbound conformation. Nonetheless, the folded LH in p27 remains tightly bound to the complex, especially on the interface with Cyclin A [20], providing the option for p27 to perform other functions in a partially bound conformation.

Control of the cell cycle requires flexible architectures rather than rigid assemblies that can be easily regulated, for example, by post-translational modifications and degradation. Assembly of p27 with Cdk2/Cyclin A complexes involves a set of highly specific and weak transient interactions at play with more stable interactions, manifesting via conformational selection followed by induced folding for the complete binding pathway. p27 functions through the recognition of a highly flexible disordered segment in D1 to form a pre-initiation complex, as shown by smFRET and fast kon rates, in response to the rapid information flow in the cell. If the interaction appears to be favorable, further steps take place,

and LH and D2 in p27 adapt to the complex due to their structural and functional flexibility to precisely coordinate the activity of the kinase complex. The dynamics and flexibility of IDPs provide an elegant mechanism through which they may simultaneously maintain binding specificity and the ability to interact with multiple partners under specific conditions. This type of binding mode is a likely mechanism for many such regulatory IDPs containing binding motifs in disordered regions that may adopt partially or fully folded secondary structural elements upon interaction with their binding partners.

#### Materials and Methods

#### Sample preparation

p27 KID (residues 22–104) and full length (residues 1–198) constructs were prepared by inserting in the pET28a vector (Novagen) [48] as described earlier [20,49]. We substituted single or double cysteine mutations for fluorescence labeling via site-directed mutagenesis at the positions Glu40, Glu54, Glu75, and Arg93. Position 29 was a native cysteine and replaced by Alanine in all constructs where Cys29 was not used as a labeling site.

All p27 constructs along with human Cdk2 and human Cyclin A (residues 173–432) are produced in *E. coli* and purified using Ni<sup>2+</sup>-NTA affinity chromatography followed by the removal of (His)<sub>6</sub>-tag using thrombin protease (Novagen) [19]. We further purified p27 constructs by using reverse-phase HPLC. Gel filtration method was used to purify further Cdk2 and Cyclin A. Buffers containing 25 mM Tris-HCl, 100 mM NaCl, and 0.5 mM TCEP, pH 8.0, were used for all purification steps. We eluted p27 using 250 mM Imidazole in the Ni<sup>2+</sup>-NTA affinity chromatography.

For fluorescence labeling, we diluted p27 to 50-70 μM in 20 mM Tris-HCl, 10 mM NaCl, pH 8.0 (buffer A) containing additionally 10 mM DTT to reduce the cysteine residues. Directly before labeling, the DTT was removed by buffer exchange to buffer A using a PD10 column (GE Healthcare) according to the manufacturer's instruction. Next, we labeled each variant with Alexa Fluor 647 (acceptor) maleimide fluorophore (Invitrogen) at a 1:1 ratio followed by a 1:2 ratio of Alexa Fluor 488 (donor) maleimide fluorophore (Invitrogen). In between the two labeling steps, nonlabeled, single- and doublelabeled protein was separated using ion-exchange chromatography. Only single labeled protein was subjected to labeling with the two-fold molar excess of the donor fluorophore.

For anisotropy experiments, single cysteine variants were labeled with BODIPY-FL or Alexa Fluor 488 (Invitrogen) and purified as mentioned above.

Also, the labeled p27 was analyzed using gelfiltration chromatography to check for the absence of degradation or oligomerization.

The presence of Förster resonant energy transfer in the FRET samples was verified by observing the fluorescence emission of the donor (515 nm) and acceptor (666 nm) after excitation of the donor at 485 nm using a PerkinElmer LS55 Luminescence Spectrometer.

#### Single-molecule fluorescence measurements

We performed single-molecule fluorescence anisotropy (smFA) and Förster resonance energy transfer (smFRET) measurements by diluting labeled p27 to a pM concentration in charcoalfiltered 20 mM Tris-HCl, 10 mM NaCl, pH 8.0. pM concentration ensured we observed only a single molecule in the confocal volume at a time. We observed the proteins in solution for several hours (2 h-10 h), as previously described [20]. For maintaining kinetic equilibrium when measuring p27 bound to Cdk2/Cyclin A, we added a preformed complex with unlabeled p27 at µM concentration. Single-molecule TCSPC measurements utilize synchronized detectors to time-tag photons collected from molecules as they diffuse through a confocal volume in solution. Traversal of this confocal volume by a single fluorescently-tagged molecule, which is excited by the laser pulse, results in a rapid increase in the collected signal, called a burst [50]. This photon signal was filtered into and collected in channels corresponding to parallel or perpendicular polarizations, as well as green (donor) or red (acceptor) color. We then used data collected from each channel to calculate a multitude of parameters characterizing the behavior of the labeled molecules, including constructing fluorescence decay histograms, calculating fluorescence anisotropy as a measure of local flexibility and FRET efficiency as a distance reporter between label fluorophores (Eqs. (1)-(3)) (for FRET-labeled molecules), and more. Because we observe only a single molecule at a time, unlike ensemble methods, we can characterize the states of individual molecules during their traversal through the confocal volume. Constructing multidimensional histograms of fluorescence parameters corresponding to these bursts allows subensemble analysis of molecules with specified fluorescence characteristics [51,52].

FRET efficiency is related to the inter-fluorophore distance and can be calculated via time-resolved donor fluorescence lifetime measurements, as well as via the intensity-based approach, by calculating the ratio of acceptor photons overall fluorescence photons.

$$E = \frac{1}{1 + R_{DA}^6 / R_o^6} \tag{1}$$

$$E_{TR} = 1 - \frac{\tau_{D(A)}}{\tau_{D(0)}} \tag{2}$$

$$E_I = \frac{F_{A|D}}{F_{D|D} + F_{A|D}} \tag{3}$$

 $F_{D|D}$  and  $F_{A|D}$  are the corrected donor and acceptor fluorescence intensities under donor excitation. Background correction is performed by subtracting the relevant mean background signal in the corresponding detection channel ( $B_G$  and  $B_R$  for green and red, respectively) from the raw signal. The correction parameters  $\alpha$ ,  $\gamma$ ,  $\delta$  account for leakage of donor fluorescence into the acceptor channel, normalization of the fluorophore quantum yields, and direct excitation of the acceptor fluorophore by the donor excitation source, respectively. The calculation of these correction parameters has been described in a recent benchmark study [21]. Correction parameters used in this work are detailed in Table S7.  $\gamma = \frac{g_R}{g_G} \frac{\Phi_{E,A}}{\Phi_{E,D}}$ , with  $\frac{g_R}{g_G}$  as the ratio of red and green detection efficiencies and  $\frac{\Phi_{E,A}}{\Phi_{E,D}}$  the ratio of acceptor and donor fluorescence quantum yields, is calculated for each experiment as the quantum yield values differ for each sample.

Deviations from the static FRET line, which describes the relationship between  $E_l$  and the donor fluorescence lifetime for static FRET populations, result from the overestimation of the donor lifetime due to dynamics that cause changes in the donor lifetime during individual bursts. The traditional dynamic FRET line describes the relationship between  $E_l$  and the donor fluorescence lifetime when conformational dynamics occur between two discrete conformational states and lead to deviation from the static FRET line. We modeled the two states as Gaussian-distributed states, and each point on the dynamic FRET line represents a degree of fractional mixing between the two states, ranging from 0% of the first and 100% of the second state to 100% of the first and 0% of the second state. Both the static and dynamic lines account for variations in the observed FRET efficiency due to the fluorophore linker dynamics while tethered to the labeled molecule. We generated static and dynamic FRET lines based on the seTCSPC results using the fluorescence fitting software ChiSurf (https://github. com/Fluorescence-Tools/chisurf) as described in https://github.com/Fluorescence-Tools/chisurf/wiki/ Calculation-of-FRET-lines.

The worm-like chain (WLC) model describes how a dynamic population that exhibits WLC dynamics would diverge from the static FRET line. This model for calculation of FRET lines additionally corrects for the effects of fluorophore linker dynamics on the observed FRET efficiency. As described elsewhere [27,53] and also as previously [20], the fluorophores are coupled to the protein by a flexible linker, and thus, show Gaussian chain like characteristics. In

$$\sigma_{AV} = \sqrt{\sigma_{Donor}^2 + \sigma_{Acceptor}^2}$$

Now, we consider for the WLC-distribution (p- $_{WLC}(R_{DA})$ ) the dye-linker effects by:

$$p(R_{DA}) = \int p_{WLC}(R_{RDA}) \cdot p_L(R_L, R_{DA}) dR_{DA}$$
 (5)

where  $p_{WLC}(R_{DA})$  is given by:

$$p_{WLC}(R_{DA}) = \frac{1 - c \cdot R_{DA}^{2}}{\left(1 - R_{DA}^{2}\right)^{5/2}} e^{\left(\frac{d \cdot \kappa \cdot a \cdot b(1+b)}{1 - (bR_{DA})^{2}} R_{DA}^{2}\right)} \cdot e^{\left[\left(-\frac{3}{4} \cdot \frac{1}{\kappa} - \frac{1}{2}\right) R_{DA}^{2} + \left(-\frac{23}{64} \cdot \frac{1}{\kappa} + \frac{17}{16}\right) R_{DA}^{4} \left(-\frac{7}{64} \cdot \frac{1}{\kappa} - \frac{9}{16}\right) R_{DA}^{6}\right] \cdot \frac{1}{1 - R_{DA}^{2}}}.$$

$$I_{0}\left(\frac{-d \cdot \kappa \cdot a \cdot (1+b) R_{DA}}{1 - (bR_{DA})^{2}}\right)$$
(6)

contrast, for p27, we expect some residual and transient structures to be present. Thus, for fitting, we decouple the fluorophore motion from the motion of p27. Using the concept of accessible volumes

with 
$$a=14.054,\,b=0.473c=1-(1+(0.38 \cdot k^{-0.95})^{-5})^{-1/5}$$
 and

$$d = \begin{cases} 1 & \kappa < 1/8 \\ 1 - \frac{1}{0.177/(\kappa - 0.111) + 6.40(\kappa - 0.111)^{0.783}} & \text{otherwise} \end{cases}$$

[53], we describe the spatial probability distributions of the dyes by 3-dimensional Gaussians with uniform width for the donor  $\sigma_D$  and the acceptor  $\sigma_A$  ( $\sigma_D = \sigma_A = 6$  Å) [53]. The resulting distance distribution  $p(R_L, R_{DA})$  between the donor and the acceptor for a single conformation with a separation distance  $R_L$  is given by:

where

$$I_0$$
: Bessel – function of Order Zero

We calculated the FRET-induced donor decay of DA-populations selected from smFRET experiments, as described in reference [27]. Briefly, in a first step, the fluorescence decay of the FRET sample  $I_{DA}(t)$  is divided by the (modeled) decay of the single-labeled sample  $I_{DO}(t)$  (or from the DOnly

$$p(R_L, R_{DA}) = \begin{cases} if \ R_{DA} > 0 & \frac{R_L}{R_{DA}} \cdot [N(R_L, R_{DA}, \sigma_{AV}) - \overline{N(R_L, -R_{DA}, \sigma_{AV})}] \\ if \ R_{DA} = 0 & 2\left(\frac{R_L}{\sigma_{AV}}\right)^2 N(R_L, 0, \sigma_{AV}) \end{cases}$$
(4)

$$N(R_L, R_{DA}, \sigma_{AV}) = \frac{1}{\sqrt{2\pi}} \exp\left(-\frac{(R_L - R_{DA})^2}{2 \cdot \sigma_{AV}^2}\right)$$

and

population in smFRET experiments, respectively). Next, the DOnly fraction,  $x_{D0}$ , is subtracted, and finally, this ratio is multiplied with the time axis t to yield the FRET-induced donor decay  $\epsilon(t)$ :(7)

$$\epsilon(t) = \left(\frac{I_{DA}(t)}{I_{D0}(t)} - x_{D0}\right) *t \tag{7}$$

For an intuitive display, we converted the x-axis from time t to the critical distance  $R_{DA,c}$  by the following relation:

$$R_{DA,c} = R_0 * \left(\frac{t}{\tau_D}\right)^{1/6} \tag{8}$$

where  $R_0$  is the Förster radius of the used FRET dye pair (here 52 Å) and  $\tau_D$  the reference fluorescence lifetime of the donor fluorophore (here, 4 ns). Plotting  $\epsilon(t)$  against  $R_{DA,c}$  results in a peaking distribution, which reflects the probability density function of the underlying distance distribution of the original decay  $I_{DA}(t)$ .

For non-WLC fits of seTCSPC Donor Only (DOnly) data (Table S2), we used a multiexponential model to describe the donor fluorescence decay:

$$F(t) = F_0 \sum_{i} a_i e^{-t/\tau_D} \tag{9}$$

where F is the total number of photon counts at time t after the donor excitation pulse summed over all excitation pulse cycles,  $F_0$  is the number of photon counts immediately after excitation, and  $a_i$  are amplitudes for each exponential decay term.

For fluorescence anisotropy calculations, the Perrin equation describing the relationship between fluorescence anisotropy, fluorescence lifetime, and the rotational correlation time of a molecule is given by:

$$r = \frac{r_0}{1 + \tau/\rho} \tag{10}$$

r is the observed anisotropy,  $r_0$  is the fundamental anisotropy of the fluorophore, au is the fluorescence

lifetime using Eq. (10). Shown curves are for  $\rho=\langle \rho_G \rangle$  for each measurement. The mean anisotropy for each sample,  $\langle r_G \rangle$ , was calculated as the population-weighted average of the corresponding high and low r values in Table S1.

# Fluorescence analysis for single-molecule experiments

We carried out fluorescence analysis for smFA and smFRET using smMFD, as previously described [20,51]. We have calculated the anisotropy, distance distribution, and their corresponding uncertainties using photon distribution analysis (PDA) [24,25]. PDA utilizes multiple, differently sized time windows, as well as consideration of shot noise and background contributions, to construct accurate fluorescence parameter histograms from single-molecule data and determine the underlying populations.

The species-specific interconversion rates were detected using filtered Fluorescence Correlation Spectroscopy (fFCS) [30]. fFCS functions similarly to traditional fluorescence correlation spectroscopy, except correlations are between signals corresponding to filtered species defined by their characteristic fluorescence and fluorescence anisotropy decay characteristics. The total observed signal is treated as a linear combination of signals from constituent species, and correlations between these species exhibit increased relative contributions from kinetic transitions between species on timescales shorter than the diffusion time, increasing the ability to resolve the timescales of these fast transitions compared to traditional FCS [30]. We performed the analyses using in-house software that is available from http://www.mpc.hhu.de/software.html. fFCS curves were fit according to the following functions:

$$f = b + \frac{1}{N_{Br} \left( 1 + \frac{t}{t_{diff}} \right) \sqrt{1 + \frac{t}{(\omega_0/z_0)^2 t_{diff}}}} \left( 1 + \sum_i |AC_i| e^{-\frac{t}{t_i}} - |AC_i| \right) \left( 1 - |B| + |B| e^{-\frac{t}{t_B}} \right)$$
(11)

lifetime, and  $\rho$  is the rotational correlation time. The grey lines in Fig. 2 relate the anisotropy and rotational correlation time as a function of donor

Species Auto-correlation:

$$f = b + \frac{1}{N_{CC} \left(1 + \frac{t}{t_{diff}}\right) \sqrt{1 + \frac{t}{(\omega_0/z_0)^2 t_{diff}}}} \left(1 - CC \sum_{i} |X_i| e^{-\frac{t}{R_i}}\right) \left(1 - |B| e^{-\frac{t}{t_B}}\right), \sum_{i} |X_i| = 1$$
(12)

Species Cross-correlation:

Here, b is the correlation baseline value (typically 1), N is the average number of molecules in the confocal volume, t is the correlation time,  $\tau_D$  is the diffusion time,  $\omega_0/z_0$  is the ratio of the axial to radial dimensions of the confocal volume, and AC and X are correlation amplitudes for the corresponding decay times in exponentials. AC and X terms are of interest for dynamic changes in FRET. B in the autocorrelation accounts for photophysical effects of the dyes and in the cross-correlation for additional long-timescale processes. The  $X_i$  are the cross-correlation amplitudes normalized to 1, with the relative scaling of the cross-correlation factor CC.

# Analysis of sub-ensemble fluorescence decay histograms (seTCSPC)

The photon arrival time histograms of the donoronly (Donly) and donor-acceptor (DA) populations exported from the smFRET experiments were analyzed using different fit models using the Burst-Integrated Fluorescence Lifetime scatter-correction (BIFL-scatter) approach [50]. BIFL-scatter explicitly takes into consideration the background photons, which constitute a significant fraction of signal in single-molecule experiments. We analyzed the DA populations of both free p27 and p27 in complex with a multiexponential fit. p27 in the complex was modeled by two Gaussian distributed distances, as described previously [20]. Free p27, in contrast, was modeled using a linker-corrected worm-like chain model (WLC). We implemented the WLC model as described by reference [54] and Eqs. (5) and (6).

#### Discrete molecular dynamics simulations

Discrete Molecular Dynamics (DMD) [23] utilizes the Medusa force field with discretized potentials and implicit solvent to calculate interatomic forces in all-atom molecular dynamics simulations. The implicit solvent model employed in DMD is a CHARMM 19-based energy function and Gaussian solventexclusion model detailed in reference [55]. In this approach, charge-charge interactions are approximated by a distance-dependent dielectric constant. while self-energy contributions are handled by the exclusion model. For this study, we used the  $\pi DMD$ software package to run all-atom replica exchange simulations [56] for the full-length p27. We obtained the simulation input structure by using  $\pi DMD$  to construct the p27 sequence found at UniProtKB -P46527 as an extended chain [57]. After an initial equilibration run of 50000 time steps (~2 fs per time step), sixteen replicas of the input structure were allowed to exchange between sixteen temperature baths equally spaced from 275 K to 350 K, held at constant temperatures according to the Andersen Thermostat [58]. The exchange probability for each pair of replicas with temperatures  $T_i$  and  $T_j$  and energies  $E_i$  and  $E_j$  is given by

$$p = \min\left(1, \exp\left(\left(E_i - E_j\right) \left(\frac{1}{k_B T_i} - \frac{1}{k_B T_j}\right)\right)\right) \tag{13}$$

We calculated the exchange probability every 1000 time steps in the trajectory. The sum of simulation time from all replicas was 1.027  $\mu$ s. All data analysis was performed using VMD [37] scripts and AvTraj [33] with MdTraj [34] (Python packages). We performed simulations on the Palmetto Cluster at Clemson University.

#### Accessible volume simulations

Accessible Volume (AV) simulations were performed using the AvTraj Python package [33,34]. These AV simulations probe the geometrically accessible volume for dyes modeled by conjoined spheres attached to the labeled atom via a linker of fixed length. This volume is calculated on a grid for each frame in the simulation trajectory and sampled for each frame to obtain the mean interdye distance for that frame and build the FRET distance distributions for the entire trajectory. The Alexa dyes were modeled using the Alexa488 and Alexa 647 dye parameter sets included in the AvTraj package.

#### Data and code availability

Software for analysis of single-molecule experiments, written in house, can be downloaded from <a href="http://www.mpc.hhu.de/software.html">http://www.mpc.hhu.de/software.html</a>. The fluorescence decay histograms were analyzed using ChiSurf (https://github.com/Fluorescence-Tools/chisurf). Original data is available upon request from the authors.

#### Acknowledgments

We would like to thank Dr. Feng Ding and Dr. Nabanita Saikia for their guidance in performing rxDMD simulations. M.T. acknowledges support by a Marie Sklodowska-Curie postdoctoral fellowship (FP7 Grant 330847 — STARIDP). N.K. was supported by Clemson University Fellows. Moreover, this work was supported by the Odysseus grant G.0029.12 from Research Foundation Flanders (FWO) and grants K124670 and K131702 from the Hungarian Scientific Research Fund (OTKA) for P.T. C.A.M.S. was supported by the ERC Advanced Grant hybridFRET (671208), and H.S. acknowledges funds from Clemson University, NSF

(CAREER MCB- 1749778) and US National Institutes of Health (NIH) P20GM121342.

### Appendix A. Supplementary data

Supplementary data to this article can be found online at https://doi.org/10.1016/j.jmb.2020.02.010.

Received 22 October 2019; Received in revised form 27 January 2020; Accepted 9 February 2020 Available online 20 February 2020

## Keywords:

p27; IDP:

single molecule FRET; single molecule fluorescence anisotropy; fluorescence correlation spectroscopy; Stopped-flow kinetics;

replica exchange discrete molecular dynamic simulations

<sup>†</sup> The author is currently an employee of the European Research Council Executive Agency. The views expressed are purely those of the writer and may not in any circumstances be regarded as stating an official position of the European Commission.

#### References

- [1] R. Pancsa, P. Tompa, Structural disorder in eukaryotes, PloS One 7 (2012) e34687.
- [2] D. Piovesan, F. Tabaro, I. Micetic, M. Necci, F. Quaglia, C.J. Oldfield, et al., DisProt 7.0: a major update of the database of disordered proteins, Nucleic Acids Res. 45 (2017) D219—D227.
- [3] A.K. Dunker, I. Silman, V.N. Uversky, J.L. Sussman, Function and structure of inherently disordered proteins, Curr. Opin. Struct. Biol. 18 (2008) 756–764.
- [4] A.K. Dunker, C.J. Brown, J.D. Lawson, L.M. lakoucheva, Z. Obradovic, Intrinsic disorder and protein function, Biochemistry 41 (2002) 6573—6582.
- [5] H.J. Dyson, P.E. Wright, Coupling of folding and binding for unstructured proteins, Curr. Opin. Struct. Biol. 12 (2002) 54–60.
- [6] A. Mittal, N. Lyle, T.S. Harmon, R.V. Pappu, Hamiltonian switch metropolis Monte Carlo simulations for improved conformational sampling of intrinsically disordered regions tethered to ordered domains of proteins, J. Chem. Theor. Comput. 10 (2014) 3550–3562.
- [7] M.M. Babu, R.W. Kriwacki, R.V. Pappu, Structural biology. Versatility from protein disorder, Science 337 (2012) 1460–1461.

- [8] M. Fuxreiter, P. Tompa, Fuzzy Complexes: a More Stochastic View of Protein Function, Springer, Fuzziness, 2012, pp. 1–14.
- [9] A.L. Darling, V.N. Uversky, Intrinsic disorder and posttranslational modifications: the darker side of the biological dark matter, Front. Genet. 9 (2018) 158.
- [10] U.B. Choi, S. Xiao, L.P. Wollmuth, M.E. Bowen, Effect of Src kinase phosphorylation on disordered C-terminal domain of N-methyl-D-aspartic acid (NMDA) receptor subunit GluN2B protein, J. Biol. Chem. 286 (2011) 29904—29912.
- [11] Z. Monahan, V.H. Ryan, A.M. Janke, K.A. Burke, S.N. Rhoads, G.H. Zerze, et al., Phosphorylation of the FUS low-complexity domain disrupts phase separation, aggregation, and toxicity, EMBO J. 36 (2017) 2951–2967.
- [12] U.B. Choi, J.J. McCann, K.R. Weninger, M.E. Bowen, Beyond the random coil: stochastic conformational switching in intrinsically disordered proteins, Structure 19 (2011) 566–576.
- [13] X. Lin, P. Kulkarni, F. Bocci, N.P. Schafer, S. Roy, M.Y. Tsai, et al., Structural and dynamical order of a disordered protein: molecular insights into conformational switching of PAGE4 at the systems level, Biomolecules 9 (2019).
- [14] Y. He, Y. Chen, S.M. Mooney, K. Rajagopalan, A. Bhargava, E. Sacho, et al., Phosphorylation-induced conformational ensemble switching in an intrinsically disordered cancer/ testis antigen, J. Biol. Chem. 290 (2015) 25090–25102.
- [15] L. Ou, M.B. Waddell, R.W. Kriwacki, Mechanism of cell cycle entry mediated by the intrinsically disordered protein p27Kip1, ACS Chem. Biol. 7 (2012) 678–682.
- [16] T. Hara, T. Kamura, K. Nakayama, K. Oshikawa, S. Hatakeyama, K.-I. Nakayama, Degradation of p27 Kip1 at the G0-G1 transition mediated by a Skp2-independent ubiquitination pathway, J. Biol. Chem. 276 (2001) 48937–48943.
- [17] J. Bloom, M. Pagano, Deregulated degradation of the cdk inhibitor p27 and malignant transformation, Semin. Canc. Biol. 13 (2003) 41–47.
- [18] A.A. Russo, P.D. Jeffrey, A.K. Patten, J. Massagué, N.P. Pavletich, Crystal structure of the p27Kip1 cyclindependent-kinase inibitor bound to the cyclin A–Cdk2 complex, Nature 382 (1996) 325.
- [19] E.R. Lacy, I. Filippov, W.S. Lewis, S. Otieno, L. Xiao, S. Weiss, et al., p27 binds cyclin—CDK complexes through a sequential mechanism involving binding-induced protein folding, Nat. Struct. Mol. Biol. 11 (2004) 358.
- [20] M. Tsytlonok, H. Sanabria, Y. Wang, S. Felekyan, K. Hemmen, A.H. Phillips, et al., Dynamic anticipation by Cdk2/Cyclin A-bound p27 mediates signal integration in cell cycle regulation, Nat. Commun. 10 (2019) 1676.
- [21] B. Hellenkamp, S. Schmid, O. Doroshenko, O. Opanasyuk, R. Kuhnemuth, S. Rezaei Adariani, et al., Precision and accuracy of single-molecule FRET measurements-a multilaboratory benchmark study, Nat. Methods 15 (2018) 669–676.
- [22] J. Ma, I.S. Yanez-Orozco, S. Rezaei Adariani, D. Dolino, V. Jayaraman, H. Sanabria, High precision FRET at singlemolecule level for biomolecule structure determination, JoVE 123 (2017), e55623.
- [23] D. Shirvanyants, F. Ding, D. Tsao, S. Ramachandran, N.V. Dokholyan, Discrete molecular dynamics: an efficient and versatile simulation method for fine protein characterization, J. Phys. Chem. B 116 (2012) 8375–8382.

- [24] S. Kalinin, S. Felekyan, M. Antonik, C.A. Seidel, Probability distribution analysis of single-molecule fluorescence anisotropy and resonance energy transfer, J. Phys. Chem. B 111 (2007) 10253–10262.
- [25] S. Kalinin, A. Valeri, M. Antonik, S. Felekyan, C.A. Seidel, Detection of structural dynamics by FRET: a photon distribution and fluorescence lifetime analysis of systems with multiple states, J. Phys. Chem. B 114 (2010) 7983–7995.
- [26] C. Mockel, J. Kubiak, O. Schillinger, R. Kuhnemuth, D. Della Corte, G.F. Schroder, et al., Integrated NMR, fluorescence, and molecular dynamics benchmark study of protein mechanics and hydrodynamics, J. Phys. Chem. B 123 (2019) 1453–1480.
- [27] T.O. Peulen, O. Opanasyuk, C.A.M. Seidel, Combining graphical and analytical methods with molecular simulations to analyze time-resolved FRET measurements of labeled macromolecules accurately, J. Phys. Chem. B 121 (2017) 8211–8241.
- [28] M. Böhmer, M. Wahl, H.-J. Rahn, R. Erdmann, J. Enderlein, Time-resolved fluorescence correlation spectroscopy, Chem. Phys. Lett. 353 (2002) 439–445.
- [29] I. Gregor, J. Enderlein, Time-resolved methods in biophysics. 3. Fluorescence lifetime correlation spectroscopy, Photochem. Photobiol. Sci. 6 (2007) 13–18.
- [30] S. Felekyan, S. Kalinin, H. Sanabria, A. Valeri, C.A. Seidel, Filtered FCS: species auto- and cross-correlation functions highlight binding and dynamics in biomolecules, Chem-PhysChem 13 (2012) 1036–1053.
- [31] S. Felekyan, H. Sanabria, S. Kalinin, R. Kuhnemuth, C.A. Seidel, Analyzing Forster resonance energy transfer with fluctuation algorithms, Methods Enzymol. 519 (2013) 30–85
- [32] A.K. Brewer, A.M. Striegel, Characterizing the size, shape, and compactness of a polydisperse prolate ellipsoidal particle via quadruple-detector hydrodynamic chromatography, Analyst 136 (2011) 515–519.
- [33] S. Kalinin, T. Peulen, S. Sindbert, P.J. Rothwell, S. Berger, T. Restle, et al., A toolkit and benchmark study for FRETrestrained high-precision structural modeling, Nat. Methods 9 (2012), 1218-U1129.
- [34] R.T. McGibbon, K.A. Beauchamp, M.P. Harrigan, C. Klein, J.M. Swails, C.X. Hernandez, et al., MDTraj: a modern open library for the analysis of molecular dynamics trajectories, Biophys. J. 109 (2015) 1528–1532.
- [35] M. Heinig, D. Frishman, STRIDE, A web server for secondary structure assignment from known atomic coordinates of proteins, Nucleic Acids Res. 32 (2004) W500–W502.
- [36] L. Ou, A.M. Ferreira, S. Otieno, L.M. Xiao, D. Bashford, R.W. Kriwacki, Incomplete folding upon binding mediates cdk4/Cyclin D Complex activation by tyrosine phosphorylation of inhibitor p27 protein, J. Biol. Chem. 286 (2011) 30142–30151.
- [37] W. Humphrey, A. Dalke, K. Schulten, VMD: visual molecular dynamics, J. Mol. Graph. Model. 14 (1996) 33–38.
- [38] P. Tompa, M. Fuxreiter, Fuzzy complexes: polymorphism and structural disorder in protein-protein interactions, Trends Biochem. Sci. 33 (2008) 2—8.
- [39] P. Tompa, C. Szász, L. Buday, Structural disorder throws new light on moonlighting, Trends Biochem. Sci. 30 (2005) 484—489.

- [40] E.A. Bienkiewicz, J.N. Adkins, K.J. Lumb, Functional consequences of preorganized helical structure in the intrinsically disordered cell-cycle inhibitor p27(Kip1), Biochemistry 41 (2002) 752–759.
- [41] P. Tompa, P. Csermely, The role of structural disorder in the function of RNA and protein chaperones, Faseb. J. 18 (2004) 1169–1175.
- [42] Y. Wang, J.C. Fisher, R. Mathew, L. Ou, S. Otieno, J. Sublet, et al., Intrinsic disorder mediates the diverse regulatory functions of the Cdk inhibitor p21, Nat. Chem. Biol. 7 (2011) 214–221.
- [43] P.E. Wright, H.J. Dyson, Intrinsically unstructured proteins: re-assessing the protein structure-function paradigm, J. Mol. Biol. 293 (1999) 321–331.
- [44] V.N. Uversky, What does it mean to be natively unfolded? Eur. J. Biochem. 269 (2002) 2–12.
- [45] H.J. Dyson, P.E. Wright, Intrinsically unstructured proteins and their functions, Nat. Rev. Mol. Cell Biol. 6 (2005) 197–208.
- [46] S. Otieno, C.R. Grace, R.W. Kriwacki, The role of the LH subdomain in the function of the Cip/Kip cyclin-dependent kinase regulators, Biophys. J. 100 (2011) 2486–2494.
- [47] P. Bowman, C.A. Galea, E. Lacy, R.W. Kriwacki, Thermodynamic characterization of interactions between p27(Kip1) and activated and non-activated Cdk2: intrinsically unstructured proteins as thermodynamic tethers, Biochim. Biophys. Acta 1764 (2006) 182–189.
- [48] M. Grimmler, Y. Wang, T. Mund, Z. Cilensek, E.M. Keidel, M.B. Waddell, et al., Cdk-inhibitory activity and stability of p27Kip1 are directly regulated by oncogenic tyrosine kinases, Cell 128 (2007) 269–280.
- [49] M. Grimmler, Y. Wang, T. Mund, Z. Cilenšek, E.-M. Keidel, M.B. Waddell, et al., Cdk-inhibitory activity and stability of p27Kip1 are directly regulated by oncogenic tyrosine kinases, Cell 128 (2007) 269–280.
- [50] J.R. Fries, L. Brand, C. Eggeling, M. Köllner, C.A.M. Seidel, Quantitative identification of different single molecules by selective time-resolved confocal fluorescence spectroscopy, J. Phys. Chem. 102 (1998) 6601–6613.
- [51] E. Sisamakis, A. Valeri, S. Kalinin, P.J. Rothwell, C.A. Seidel, Accurate single-molecule FRET studies using multiparameter fluorescence detection, Methods Enzymol. 475 (2010) 455–514.
- [52] G. Hamilton, H. Sanabria, Chapter 6 multiparameter fluorescence spectroscopy of single molecules, in: C.K. Johnson (Ed.), Spectroscopy and Dynamics of Single Molecules, Elsevier, 2019, pp. 269–333.
- [53] S. Sindbert, S. Kalinin, H. Nguyen, A. Kienzler, L. Clima, W. Bannwarth, et al., Accurate distance determination of nucleic acids via Forster resonance energy transfer: implications of dye linker length and rigidity, J. Am. Chem. Soc. 133 (2011) 2463—2480.
- [54] N.B. Becker, A. Rosa, R. Everaers, The radial distribution function of worm-like chains, Eur. Phys. J. E Soft Matter 32 (2010) 53–69.
- [55] T. Lazaridis, M. Karplus, Effective energy function for proteins in solution, Proteins 35 (1999) 133–152.
- [56] Y. Okamoto, Generalized-ensemble algorithms: enhanced sampling techniques for Monte Carlo and molecular dynamics simulations, J. Mol. Graph. Model. 22 (2004) 425–439.
- [57] C. UniProt, UniProt: a worldwide hub of protein knowledge, Nucleic Acids Res. 47 (2019) D506–D515.

- [58] H.C. Andersen, Molecular dynamics simulations at constant pressure and/or temperature, J. Chem. Phys. 72 (1980) 2384–2393.
- [59] S.G. Sivakolundu, D. Bashford, R.W. Kriwacki, Disordered p27Kip1 exhibits intrinsic structure resembling the Cdk2/ cyclin A-bound conformation, J. Mol. Biol. 353 (2005) 1118–1128.
- [60] P. Virtanen, R. Gommers, T.E. Oliphant, M. Haberland, T. Reddy, D. Cournapeau, et al., SciPy 1.0-fundamental algorithms for scientific computing in Python, ArXiv (2019) 10121, abs/1907.
- [61] D.S. Goodsell, L. Autin, A.J. Olson, Illustrate: Software for Biomolecular Illustration, Structure 27 (11) (2019) 1716–1720, https://doi.org/10.1016/j.str.2019.08.011.

## **Supplementary information**

# Specific Conformational Dynamics and Expansion Underpin a Multi-Step Mechanism for Specific Binding of p27 with Cdk2/Cyclin A

Maksym Tsytlonok<sup>1</sup>, Katherina Hemmen<sup>2,3</sup>, George Hamilton<sup>4</sup>, Narendar Kolimi<sup>4</sup>, Suren Felekyan<sup>2</sup>, Claus A. M. Seidel<sup>2</sup>, Peter Tompa<sup>1</sup>, and Hugo Sanabria<sup>2,4,\*</sup>

<sup>1</sup>VIB Center for Structural Biology, Vrije Universiteit Brussel, Brussels, Belgium.

<sup>&</sup>lt;sup>2</sup>Lehrstuhl für Molekulare Physikalische Chemie, Heinrich-Heine-Universität, 40225 Düsseldorf, Germany.

<sup>&</sup>lt;sup>3</sup>Rudolf Virchow Center for Experimental Biomedicine, University of Würzburg, 97078 Würzburg, Germany.

<sup>&</sup>lt;sup>4</sup>Department of Physics and Astronomy, Clemson University, Clemson, SC, 29634, USA.

<sup>\*</sup> Correspondence: hsanabr@clemson.edu

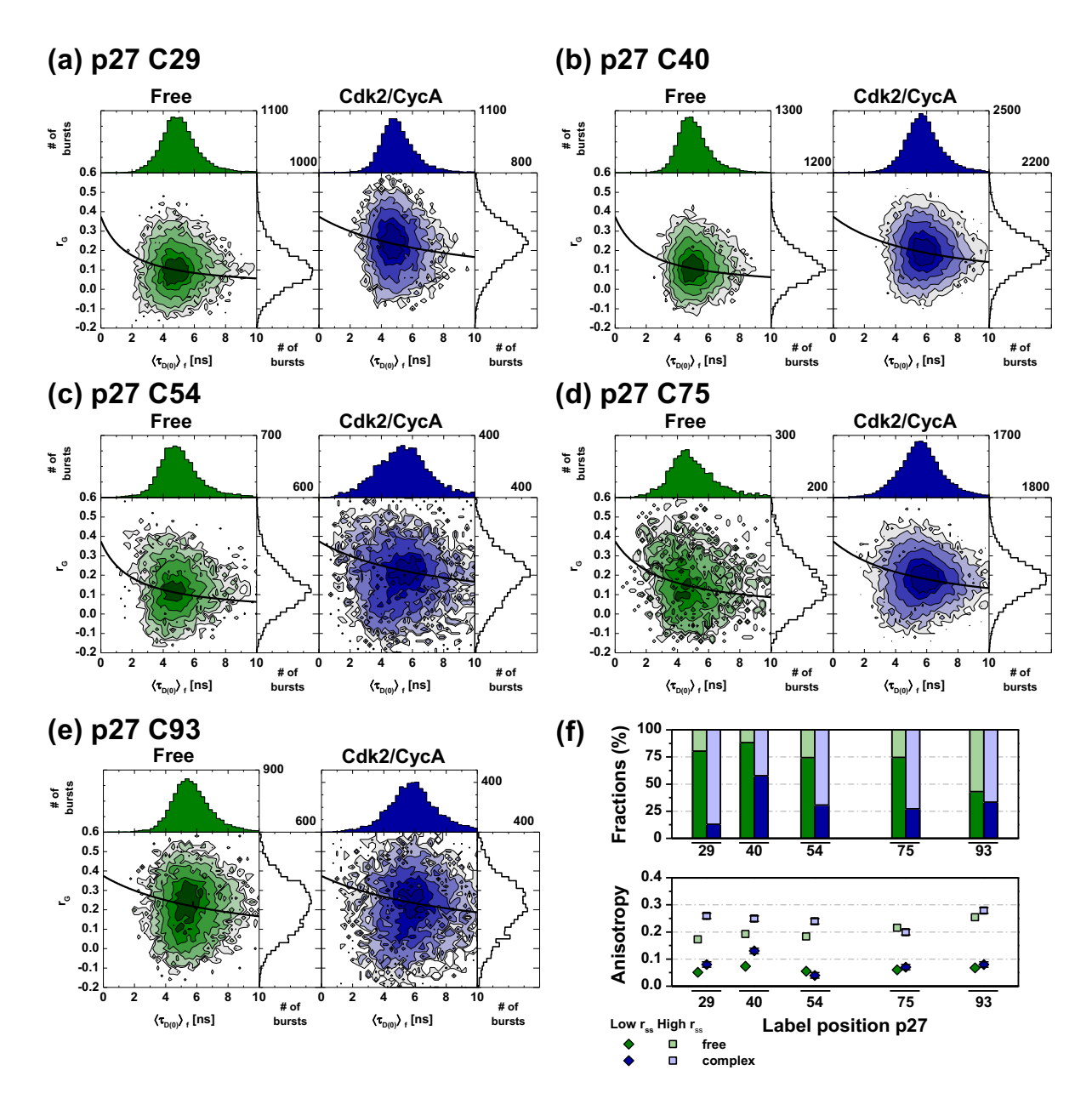


Figure S1. smFA 2D histograms of p27 single cystein variants free and in complex with Cdk2/Cyclin A. (a-f) The average fluorescence lifetime  $(\langle \tau_{D(A)} \rangle_f)$  of the BODIPY label on the x-axis vs. scatter-corrected anisotropy  $(r_D)$  on the y-axis are shown. One-dimensional frequency histograms along the axis and number of bursts at the right top corner are shown for each. In black, the Perrin equation is added through the center of the population to guide the eye. (f) Anisotropy and respective fractions for p27 free and bound to Cdk2/Cyclin A give information about local dynamics for the molecule based on global fits using PDA for three time windows  $(\Delta t = 1, 2, \text{ and } 3 \text{ ms})$ . The corresponding fractions and anisotropy values  $(r_s)$  for the Low and High  $r_s$  are presented in dark and light colors, respectively. Fit results are collected in Table S1.

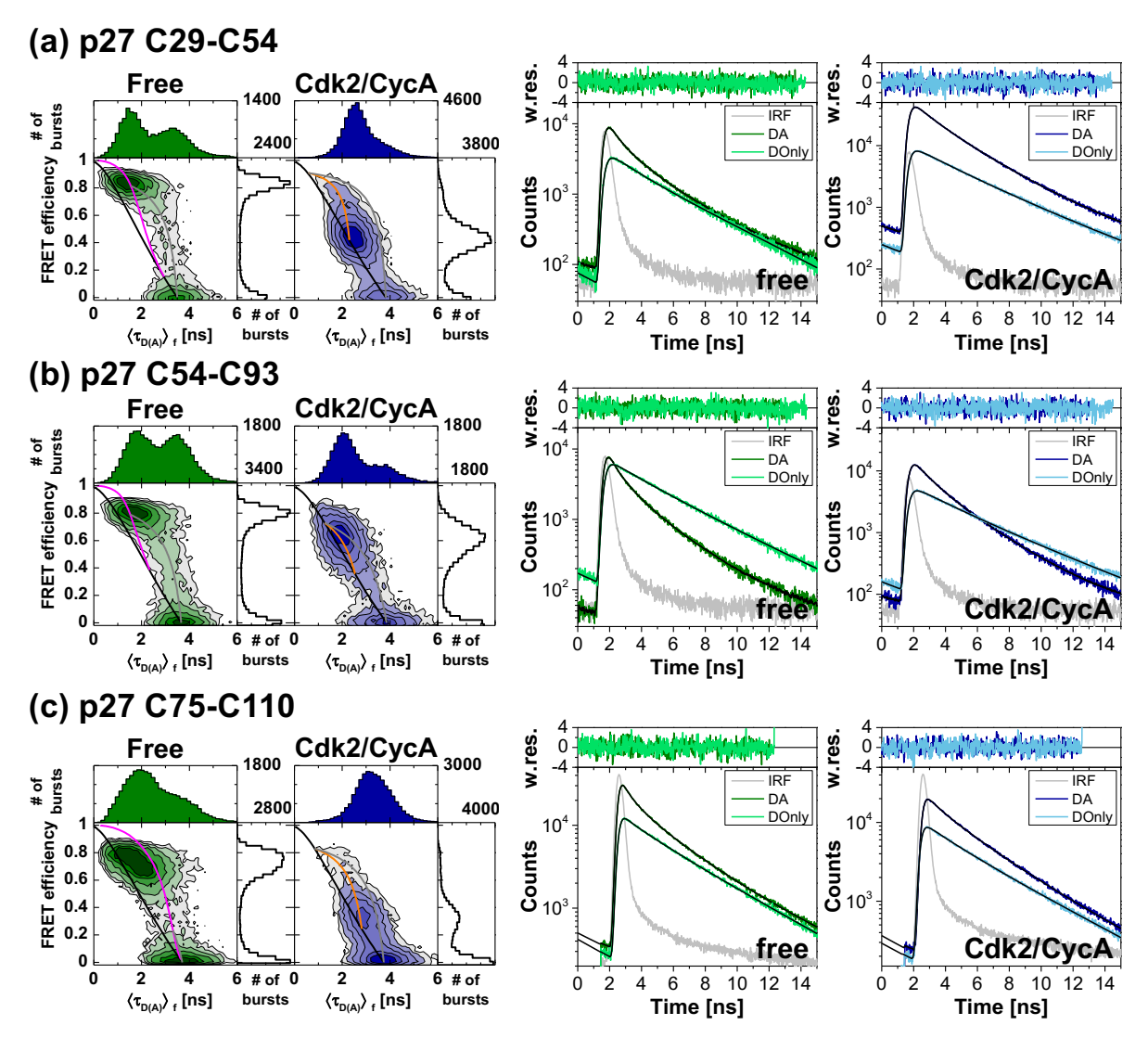
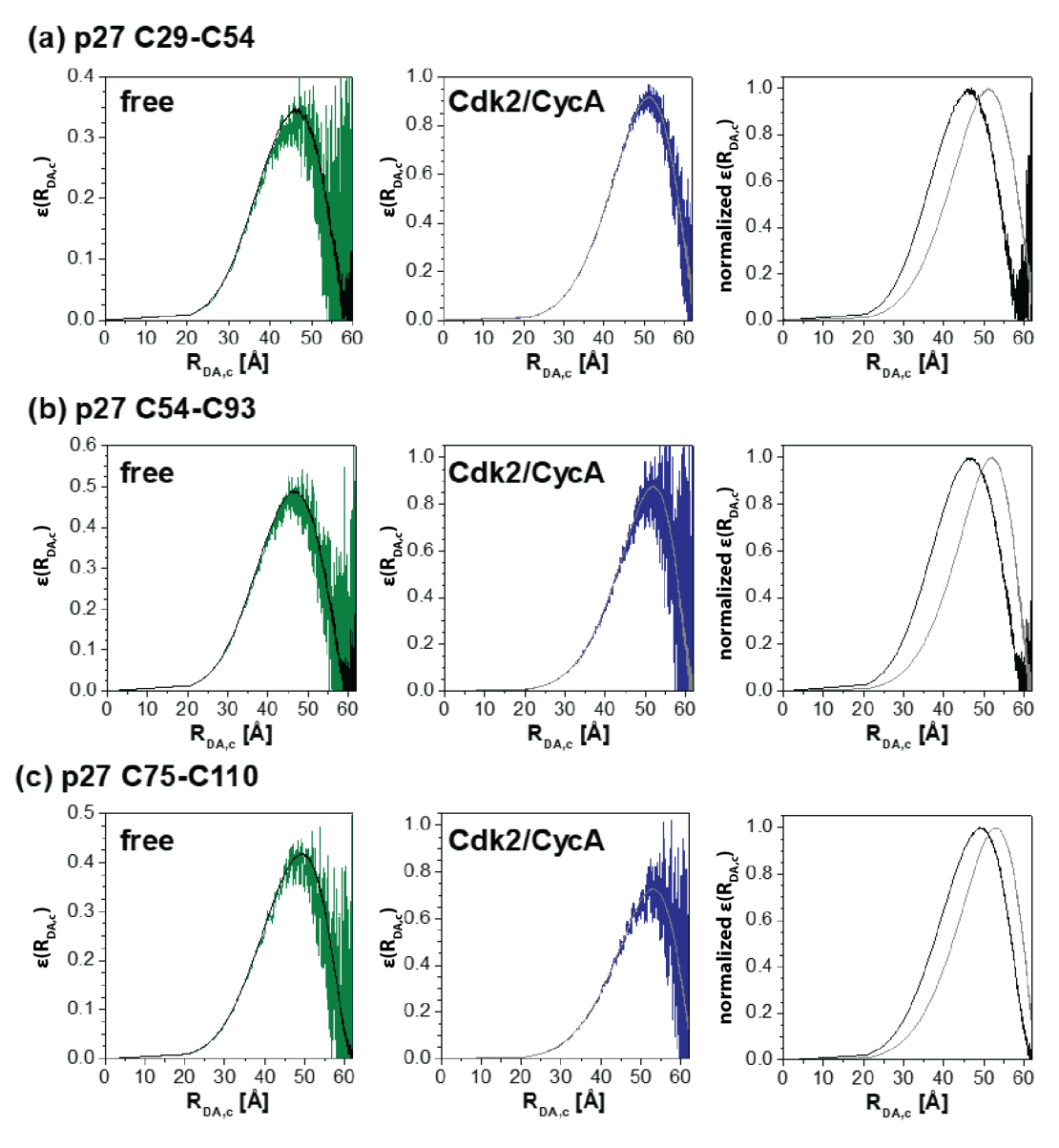
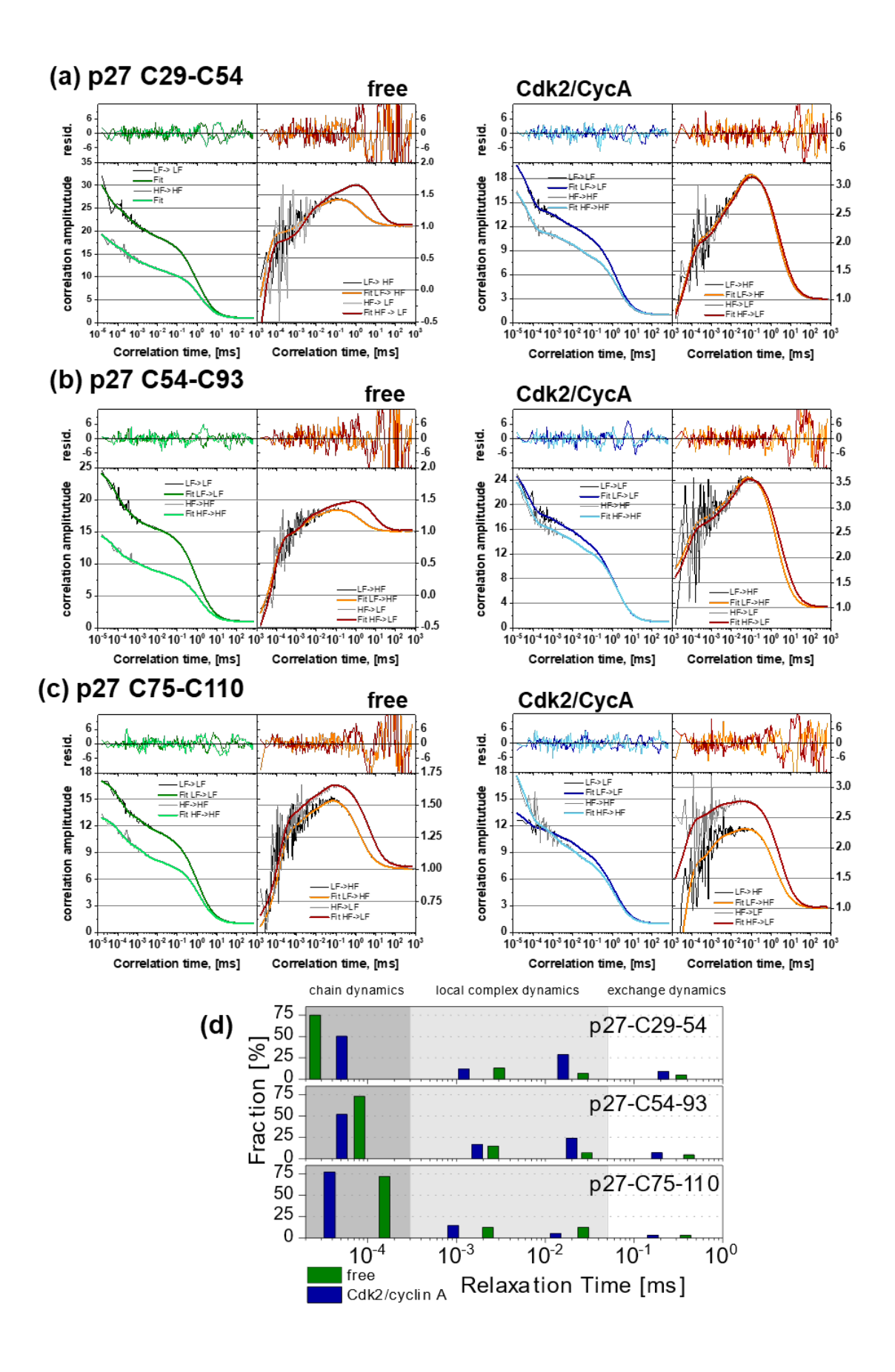


Figure S2. smFRET efficiency and sub-ensemble fluorescence decays for p27 double cysteine variants free and in complex with Cdk2/Cyclin A. (Left) The 2D histogram shows that the FRET efficiency E is decreasing from free (green) to the complex-bound form (blue). The average fluorescence lifetime ( $\langle \tau_{D(A)} \rangle_f$ ) are shown on the x-axis and FRET efficiency E on the y-axis (left). For each FRET indicator, 1D frequency histograms along the axis and number of bursts at the right top corner are shown. In black the static FRET line and in grey the bleaching/folding line for both conditions is shown, while for the free p27 we added the dynamic WLC line (magenta) and for the Cdk2/Cyclin A bound p27 the dynamic Gaussian distances line (orange). (Middle, Right) Time resolved fluorescence decays for extracted DA (dark green/blue) and DOnly populations (light green/blue) are shown. Instrument response function (IRF) is shown in grey. Weighted residuals for the respective fit model (multiexponential for DOnly, WLC for free p27 and Gaussian distances for bound p27) are shown on top. All burst from the 2D histograms below E of  $\sim 0.18$  were considered to belong to the DOnly population, i.e. either missing an active acceptor and/or a too far D-A distance to allow for FRET to happen. Details see Methods and Supporting Methods, fit results are summarized in Table S2.



**Figure S3. FRET-induced donor decays**  $\varepsilon$ (t) for seTCSPC analysis. (Left) WLC fit of DA-population, in green the raw data and in black the fit is shown. (Middle) Fit of two Gaussian distributed distances for p27 in complex with Cdk2/Cyclin A, in blue the raw data and in light grey the fit is shown. (Right) Normalized  $\varepsilon$ (t) for free (black) and bound (light grey) p27 for easier comparison. All p27 FRET variants show a shift to longer distances when bound to Cdk2/Cyclin A and a decreased width in distribution. Fit results are summarized in Table S2.



**Figure S4. Filtered FCS species-specific auto and cross correlation functions of smFRET for p27 double cysteine variants free and bound to Cdk2/Cyclin A.** Filtered FCS auto (left panels) and cross (right panel) correlations for a) p27 C29-C54, b) p27 C54-C93 and c) p27 C75-C110. Filters were selected by "burstwise" selection based on the FRET efficiency arbitrary cutoffs to select for low-FRET (LF) or high-FRET (HF) populations. The integrated fluorescence of these bursts corresponds to two independent species. The two sCCF (right, LF-> HF and HF->LF) and the sACF (LF->LF and HF->HF) where fitted globally as described in [1]. Residuals of the fits for sACF and sCCF are shown at the top of each correlation curve. (d) Fractions of the relaxation times. Fit results are summarized in Table S3.

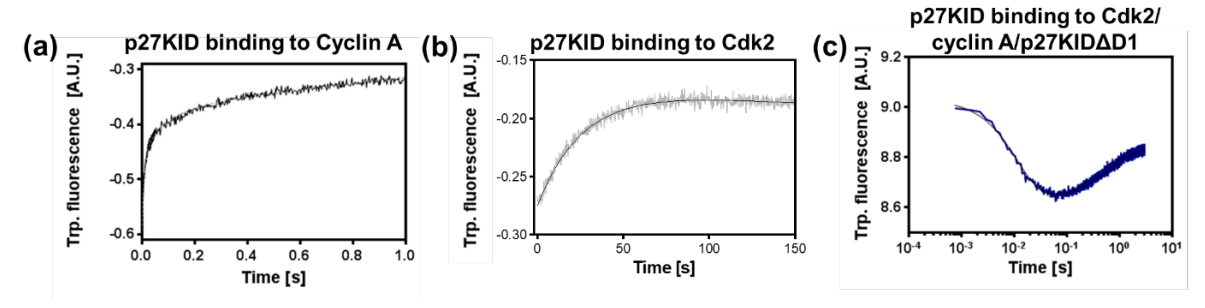
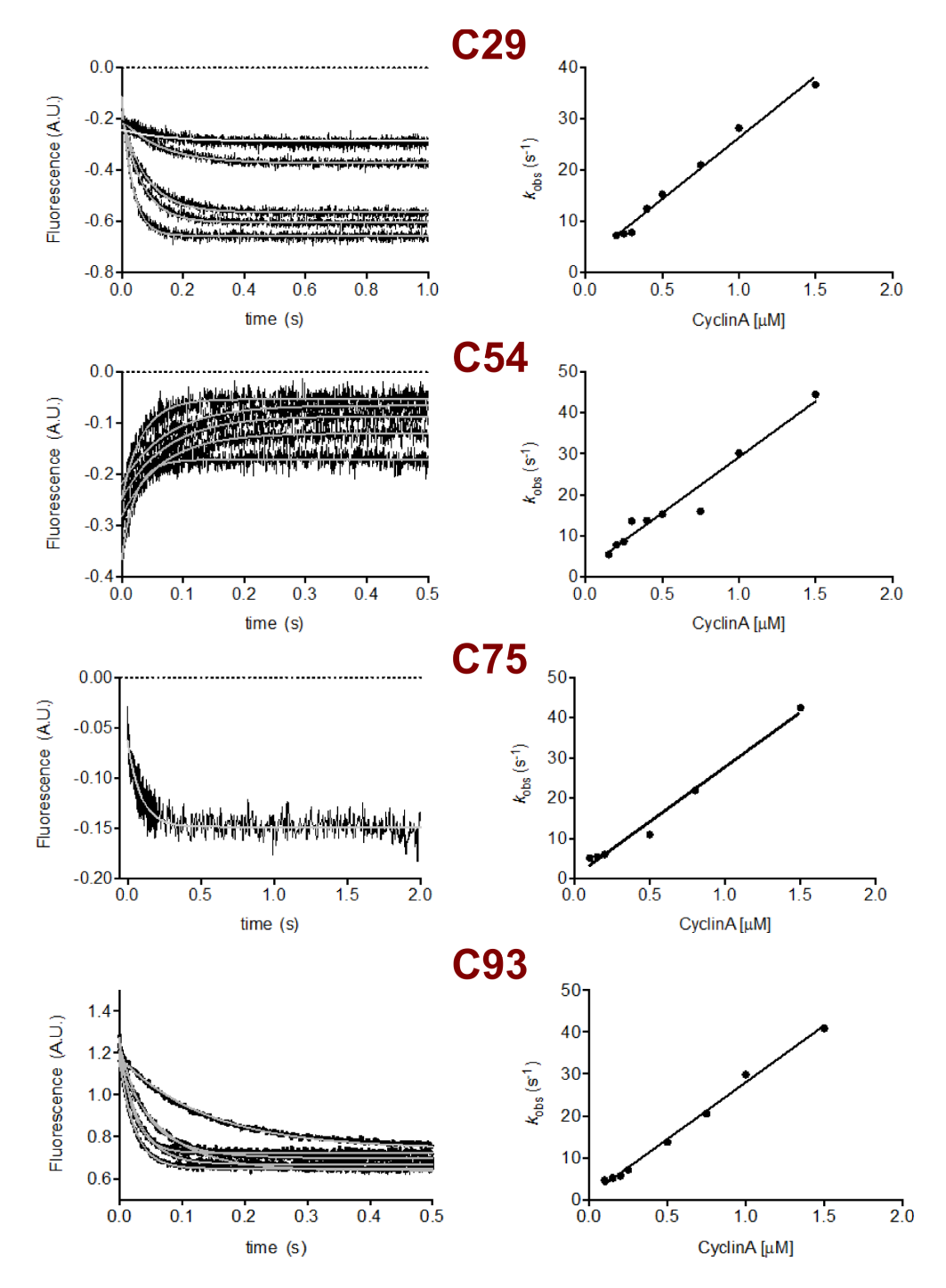


Figure S5. Tryptophan fluorescence during binding experiments for the interaction of p27KID with Cyclin A, Cdk2, and in ternary complex of Cdk2/Cycline A/p27KIDΔD1. a) Intrinsic tryptophan fluorescence increases with a very fast phase upon binding of p27KID to Cyclin A, followed by a slower phase, indicating fast initial binding followed by internal configurational changes. b) Fluorescence increases mono-exponentially for the interaction of p27KID with Cdk2. c) Tryptophan fluorescence shows a rapid decrease and a slow increase in the binding traces upon the interaction of p27KID with Cdk2/cyclinA/p27KIDΔD1 complex.



**Figure S6. The association reactions and kinetics for the interaction of fluorescently labeled p27KID with Cyclin A.**For these experiments, we labeled residues in and near the KID region of p27 with BODIPY-FL, namely sites C29, C40, C54, C75, and C93, mutated to cysteines (Fig. 1). Although the C54, C75 and C93 sites are not in the binding region of Cyclin A, the kinetic reaction shows a significant change in the fluorescence upon binding. The increased fluorescence for C54 in contrast to the other positions represents a different structural arrangement in the LH domain of p27 KID.

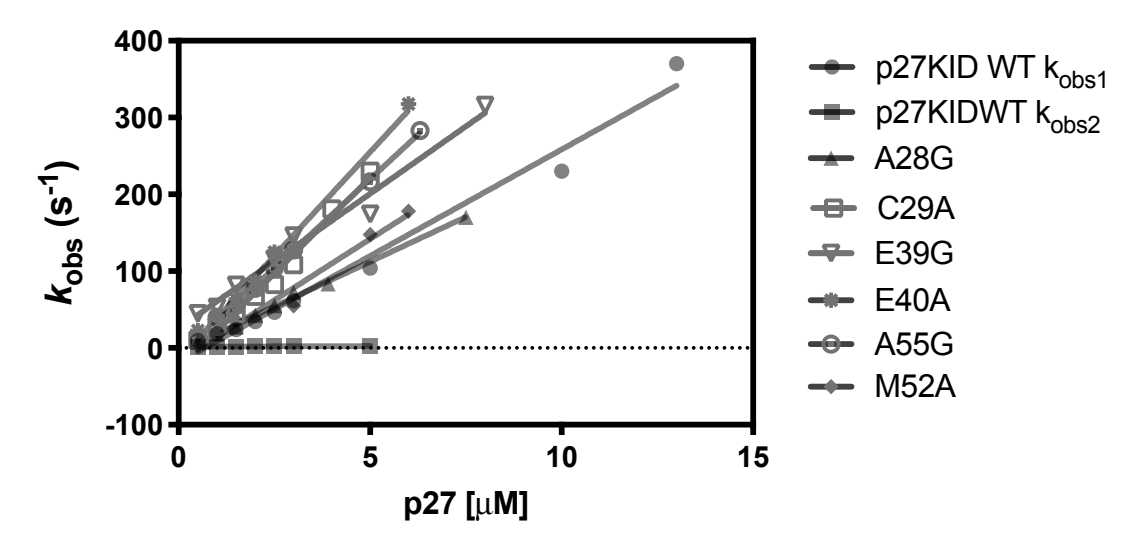


Figure S7. Binding kinetics study for the initial interaction of p27 with cyclin A is performed for different mutants of p27 by tryptophan fluorescence. The mutants in p27, A28G, C29A & E39G (located in D1) and E40A, M52A & A55G (located in LH), do not show any significant effect on the first, very fast or the second, slow rate constants.

## Table S1. smFA fit parameters for free p27and bound to Cdk2/Cyclin A.

a) Fit parameter for two state model. Uncertainties were estimated by calculating the  $\chi r^2$  distribution resulting from variation of each fit parameter and using twice the standard deviation as the uncertainty to establish a 95 % confidence interval. Parameters were varied by sampling a normal distribution centered at the mean (fit) values given in the table.

Residue	free p27	at the mean (m) v		p27 Cdk2/Cy	clin A	
number	Anisotropy (Fr	raction (%))	$\chi_{\rm r}^2$	Anisotropy (I	Fraction (%))	$\chi_{\rm r}^2$
number	Low r <sub>G</sub>	High r <sub>G</sub>		Low r <sub>G</sub> High r <sub>G</sub>		
29	0.05±0.004	0.17±0.010	1.12	$0.08\pm0.008$	0.26±0.002	1.26
29	$(80.5\pm4.0)$	(19.5±16.4)	1.12	$(12.9\pm10.8)$	(87.1±1.6)	1.20
40	0.07±0.002	0.19±0.014	1.22	0.13±0.006	0.25±0.006	1.54
40	(88.3±2.7)	(11.7±20.4)	1.22	$(57.7\pm6.9)$	$(42.3\pm9.5)$	1.54
54	0.06±0.004	0.18±0.010	1.32	$0.04\pm0.008$	0.23±0.004	1.45
34	$(74.5\pm4.8)$	(25.5±14.1)	1.32	$(30.8\pm8.4)$	(69.2±4.9)	1.43
75	0.06±0.0006	0.22±0.012	0.94	0.07±0.010	0.20±0.004	1.26
73	$(74.6\pm5.1)$	(25.4±14.9)	0.94	$(27.2\pm13.2)$	(72.8±4.9)	1.20
02	0.07±0.004	0.26±0.004	1.68	0.08±0.008	0.28±0.004	1.18
93	$(43.1\pm4.2)$	$(56.9\pm3.2)$	1.00	$(33.3\pm7.8)$	(66.7±3.9)	1.10

b) Comparison of average Anisotropy:  $(\langle r_G \rangle = b_1 r_{G,Low} + b_2 r_{G,High})$  and average rotational correlation time  $(\langle \rho_D \rangle = b_1 \rho_{G,Low} + b_2 \rho_{G,High})$ , where  $\rho_{G,Low}$  and  $\rho_{G,High}$  have been calculated by the Perrin equation  $(r_0/r_x = 1 + \tau_G/\rho_{G,x})$ . The overall tumbing of the observed molecule is reflected by  $\langle r_G \rangle$ . For a larger molecule,  $\langle r_G \rangle$  is larger. Uncertainties were propagated from a) according to the propagation rule  $\sigma_x^2 = \sum_i (\frac{dx}{dy_i})^2 \sigma_{y_i}^2$ .

Comples	Free		Cdk2/Cyclin	A
Samples	$\langle r_G \rangle$	$\langle \rho_G \rangle$ [ns]	$\langle r_G \rangle$	$\langle \rho_G \rangle$ [ns]
p27 C29	$0.07 \pm 0.028$	1.44±0.75	$0.24\pm0.010$	9.31±0.360
p27 C40	$0.09\pm0.039$	$1.64\pm1.17$	$0.18\pm0.026$	6.45±1.150
p27 C54	$0.09\pm0.026$	$1.93 \pm 0.70$	$0.18\pm0.012$	$7.05\pm0.530$
p27 C75	$0.10\pm0.033$	2.77±1.17	$0.16\pm0.014$	$5.20\pm0.410$
p27 C93	$0.17 \pm 0.009$	8.11±0.54	$0.21\pm0.013$	11.51±0.93
Average	0.10	3.18	0.19	7.90
stdev	0.02	0.87	0.02	0.68

## Table S2. seTCSPC fit parameters for free samples.

a) Fluorescence lifetime fit for DOnly-labeled molecules free in solution

Sample free	$\tau_{I}$ [ns]	<i>x</i> <sub>1</sub>	$\tau_2$ [ns]	<i>x</i> <sub>2</sub>	τ <sub>3</sub> [ns]	<i>X</i> 3	$\langle \tau_f \rangle$ [ns]	$\langle \tau_x \rangle$ [ns]	$\chi_{\rm r}^2$
p27 C29 C54	3.80	0.669	1.21	0.331			3.45	2.94	0.99
p27 C54 C93	3.75	0.762	1.21	0.238			3.52	3.15	1.08
p27 C75 C110	4.00	0.626	2.43	0.132	1.33	0.242	3.66	2.89	1.09

## b) Worm-like chain model for DA-labeled molecules free in solution

Sample free	Length* [Å]	persistence* [Å]	flexibility**	$x_{DOnly}$	χr <sup>2</sup>
p27 C29 C54	73.8 [62.0-104.0]	29.0 [19.0-40.7]	0.393	0.145	1.08
p27 C54 C93	65.7 [62.8-69.4]	30.4 [28.9-31.9]	0.463	0.060	1.14
p27 C75 C110	67.7 [63.0-73.0]	41.4 [36.0-49.0]	0.612	0.268	1.21

<sup>\*</sup>values in brackets show show 95 % confidence interval

## b) Maximum and width of FRET-induced donor decay

Comple	free		Cdk2/Cyclin A complex				
Sample	Maximum [Å]	width* [Å]	Maximum [Å]	width* [Å]			
p27 C29 C54	46.8	19.0	51.2	18.5			
p27 C54 C93	46.9	18.5	52.1	15.8			
p27 C75 C110	48.9	19.0	53.1	17.0			

<sup>\*</sup>width is determined at 50 % of the maximal height of the converted FRET-induced donor decay curve

<sup>\*\*</sup>flexibility is defined as the ratio of persistence length divided by total length

**Table S3.**a) Relaxation rate constants obtained from filteredFCS fit for free p27 and bound to Cdk/Cyclin A. Data was analysed as described prayiously [1]

previ	ousiy [1].	1	r		1			1	1			1	1	1	ı	1
Correlati	on	b	$N_{CC}/N_{Br}$	$t_{diff}[ms]$	$\omega_0/z_0$	CC	$t_{RI}$ [ $\mu$ s]	$X_{l}/AC_{l}$	$t_{R2}$ [µs]	$X_2/AC_2$	$t_{R3}$ [ $\mu$ s]	$X_3/AC_3$	<i>t</i> <sub>R4</sub> [μs]	$X_4/AC_4$	В	$\begin{bmatrix} t_B \\ [ ext{ms}] \end{bmatrix}$
p27 C29	C54															
Cdk2/	LF-HF HF-LF	1.01	0.37			1.24		0.52		0.17		0.24		0.07	0.10	
Cyclin	LF-LF	1.01	0.049	1.76	3.70		0.058	0.35	1.96	0.078	22.7	0.066	207	0.047	0.10	4.03
A	HF- HF	1.00	0.060					0.37		0.062		0.10		0.023	0.00	
	LF-HF	1.00	1.86			4.94		0.75		0.13		0.069		0.049	0.16	
	HF-LF	1.00	0.30			5.72						0.009			0.04	
free	LF-LF	0.99	0.030	1.36	6.93		0.022	0.23	2.63	0.080	23.1	0.038	297	0.073	0.01	5.12
	HF- HF	0.97	0.049					0.18		0.087		0.069		0.005	0.81	
p27 C54	C93															
Cdk2/	LF-HF HF-LF	1.00	0.34			0.82		0.50		0.12		0.29		0.09	0.01	-
Cyclin	LF-LF	1.02	0.20	1.77	3.42	0.89	0.058	0.30	1.39	0.075	18.3	0.086	247	0.084	0.44	5.76
A	HF- HF	1.01	0.041	1.//	3.42		0.030	0.35	1.37	0.065	10.5	0.096	247	0.033	0.05	3.70
	LF-HF	1.01	2.29			4.60		0.72		0.15		0.07		0.05	0.12	
	HF-LF	1.00	0.43			4.66		0.73		0.15		0.07		0.05	0.00	
free	LF-LF	1.00	0.04	1.29	4.68		0.070	0.22	2.27	0.05	25.7	0.03	363	0.08	0.00	4.96
	HF- HF	1.01	0.07					0.25		0.10		0.07		0.00	0.79	

p27 C75	C110															
	LF-HF	1.00	0.69			2.30		0.77		0.14		0.05		0.04	0.00	
Cdk2/	HF-LF	1.01	0.35			0.96		0.77		0.14		0.03		0.04	0.35	
Cyclin	LF-LF	1.01	0.076	1.52	4.05		0.043	0.17	1.06	0.072	15.1	0.11	188	0.10	0.03	2.53
A	HF- HF	1.00	0.053					0.39		0.12		0.088		0.049	0.10	
	LF-HF	1.01	1.67			1.91		0.72		0.12		0.12		0.04	0.00	
	HF-LF	1.02	0.57			1.68		0.72		0.12		0.12		0.04	0.61	
free	LF-LF	1.01	0.06	1.29	6.71		0.13	0.24	1.96	0.11	23.4	0.05	331	0.07	0.13	3.80
	HF- HF	1.01	0.08					0.24		0.16		0.06		0.01	0.06	

b) Errors calculated for a). Errors were calculated by simultaneously sampling all parameters from normal distributions centered at each fit value, calculating the  $\chi^2$  distribution for all sampled paramer values, and using the F-test for the ratio of sampled curve  $\chi^2$  values to the  $\chi^2$  value for the curves corresponding to the value in a) to define the 95% confidence interval.

Correlation	on	b	N <sub>CC</sub> /N <sub>Br</sub>	$t_{diff}[ms]$	$\omega_0/z_0$	CC	$t_{RI}$ [µs]	$X_1/AC_1$	$t_{R2}$ [µs]	$X_2/AC_2$	$t_{R3}$ [µs]	$X_3/AC_3$	<i>t</i> <sub>R4</sub> [μs]	$X_4/AC_4$	В	$t_B$ [ms]
p27 C29	C54															
Cdk2/	LF-HF HF-LF	0.18	0.20			0.11		0.03		0.10		0.14		0.01	0.03	
Cyclin	LF-LF	0.06	0.01	0.23	0.47		0.04	0.01	0.82	0.01	3.24	0.01	49.65	0.02	0.01	1.02
A	HF- HF	0.01	0.02					0.01		0.01		0.01		0.02	0.00	
	LF-HF	0.03	0.71			0.47		0.21		0.05		0.01		0.02	0.06	
	HF-LF	0.24	0.09			0.52		0.21		0.03		0.01		0.02	0.01	
free	LF-LF	0.35	0.07	0.30	0.54		0.03	0.01	0.28	0.03	2.78	0.03	92.76	0.01	0.01	0.79
	HF- HF	0.01	0.02					0.01		0.01		0.05		0.01	0.09	

p27 C54	C93															
Cdk2/	LF-HF HF-LF	0.08	0.10 0.04			0.33		0.24		0.05		0.17		0.06	0.01	
Cyclin	LF-LF	0.01	0.01	.16	0.70		0.04	0.01	0.61	0.01	2.93	0.01	52.10	0.01	0.02	1.44
A	HF- HF	0.01	0.01					0.01		0.01		0.01		0.01	0.02	
	LF-HF	0.05	0.08			0.23		0.03		0.11		0.02		0.01	0.03	
	HF-LF	0.07	0.08			0.17				0.11					0.19	
free	LF-LF	0.26	0.01	0.51	3.02		0.04	0.06	0.44		5.60	0.03	23.87	0.08	0.38	1.76
	HF- HF	0.24	0.01					0.11				0.07		0.01	0.32	
p27 C75	C110															
	LF-HF	0.41	0.02			0.29		0.17		0.02		0.02		0.01	0.01	
Cdk2/	HF-LF	0.43	0.13			0.89									0.19	
Cyclin	LF-LF	0.03	0.01	0.19	0.98		0.03	0.01	0.60	0.01	5.55	0.01	54.45	0.02	0.02	0.98
A	HF- HF	0.06	0.01					0.01		0.01		0.01		0.01	0.01	
	LF-HF	0.10	0.92			0.28		0.36		0.03		0.03		0.03	0.01	
	HF-LF	0.06	0.48			0.44		0.30		0.03		0.03		0.03	0.60	
free	LF-LF	0.39	0.01	0.22	1.09		0.03	0.13	0.67	0.08	6.39	0.02	81.26	0.04	0.13	1.79
	HF- HF	0.48	0.01					0.01		0.01		0.01		0.01	0.06	

Table S4. Radii of hydration (determined from smFRETmeasurements) and gyration.

	29-54	54-93	75-110	Simulation
R <sub>h</sub> * [Å]	18.86	17.90	17.90	
R <sub>g</sub> [Å]				36.28

<sup>\*</sup>Values for  $R_h$  calculated according to  $R_h$ =4 $k_B$   $\tau_D$  T/(6 $\pi\eta\omega^2$ ), with T=298.15 K,  $\tau_D$  the diffusion time for each sample,  $\eta$ =0.85 mPa\*s, and  $\omega^2$ =73900 nm² the square of the width of the confocal volume, determined by measuring the diffusion time of a standard sample with known diffusion time (Rhodamine-110, D = 4.7 $\times$ 10<sup>-6</sup> cm²/s).\

Table S5. Kinetic parameters determined by rapid mixing experiments.

Interacting molecules	$K_a[\mathbf{M}^{\text{-1}}\mathbf{s}^{\text{-1}}]$
p27KID + Cyclin A	$5.0 \times 10^7$
p27KID + Cdk2	$1.0 \times 10^{-2}$
p27KID + Cdk2/Cyclin A	$3.5 \times 10^7$
p27KIDΔD1 + Cyclin A	-
$p27KID\Delta D1 + Cdk2$	1.5x10 <sup>-2</sup>
p27KIDΔD1 + Cdk2/Cyclin A	$5.0 \times 10^{-2}$
p27KID + Cdk2/Cyclin A /p27KIDΔD1	$1.6 \times 10^7$

Table S6. Multiple Gaussian Fits for Rg.

Number of Gaussians	Means [Å]	Amplitudes	Standard Deviation [Å]	p-Value
1	34.8	1	15.9	0.85
2	28.1, 43.5	0.58, 0.42	7.1, 10.6	0.91
3	23.8, 30.0, 44.2	0.22, 0.44, 0.34	3.6, 6.4, 9.8	0.97

## Table S7 Correction parameters for smFA and smFRET experiments

Correction parameters are calculated and implemented as described in [2]

Sample	Correction Parameter	Value
All samples		
	Ratio of green vs. red detection efficiencies	0.8
	$(g_{\rm G}/g_{\rm R})$	
	Ratio of green perpendicular vs. parallel	1.069
	detection efficiencies (Gg)	
	Spectral cross-talk, α	1.7 %
	Direct acceptor exchitation, β	1.3 %
	Optical element depolarization factor, l <sub>1</sub>	0.0176
	Optical element depolarization factor, l <sub>2</sub>	0.0526
All free single-		
labeled BODIPY		
for smFA		
	Mean green channel background signal, B <sub>G</sub>	0.55 kHz

All complex single-		
labeled BODIPY		
for smFA		
	Mean green channel background signal, B <sub>G</sub>	1.07 kHz
p27-C29-C54 free	Tream groom onamier outing round organic, 20	Tio / RILL
P=/ C=/ CC I II CC	Mean green channel background signal, B <sub>G</sub>	1.62 kHz
	Mean red channel background signal, B <sub>R</sub>	1.03 kHz
	Donor fluorophore quantum yield, $\Phi_{F,D}$	0.61
	Acceptor fluorophore quantum yield, $\Phi_{F,A}$	0.46
p27-C54-C93 free	receptor indorophore quantum yierd, $\Psi_{\Gamma,A}$	0.10
par ce i ese nee	Mean green channel background signal, B <sub>G</sub>	1.62 kHz
	Mean red channel background signal, B <sub>R</sub>	1.03 kHz
	Donor fluorophore quantum yield, $\Phi_D$	0.66
	Acceptor fluorophore quantum yield, $\Phi_{F,A}$	0.46
p27-C75-C110 free	receptor fractophore quantum yield, \$1,4	0.10
par era errance	Mean green channel background signal, B <sub>G</sub>	0.65 kHz
	Mean red channel background signal, B <sub>R</sub>	0.42 kHz
	Donor fluorophore quantum yield, $\Phi_{F,D}$	0.69
	Acceptor fluorophore quantum yield, $\Phi_{F,A}$	0.42
p27-C29-C54 +	receptor fractophore quantum yield, ‡ r,A	0.12
Cdk2/Cyclin A		
	Mean green channel background signal, B <sub>G</sub>	1.57 kHz
	Mean red channel background signal, B <sub>R</sub>	0.94 kHz
	Donor fluorophore quantum yield, $\Phi_{F,D}$	0.61
	Acceptor fluorophore quantum yield, $\Phi_{F,A}$	0.46
p27-C54-C93 +		
Cdk2/Cyclin A		
V	Mean green channel background signal, B <sub>G</sub>	1.57 kHz
	Mean red channel background signal, B <sub>R</sub>	0.94 kHz
	Donor fluorophore quantum yield, $\Phi_{F,D}$	0.61
	Acceptor fluorophore quantum yield, $\Phi_{F,A}$	0.47
p27-C75-C110 +	<u> </u>	
Cdk2/Cyclin A		
·	Mean green channel background signal, B <sub>G</sub>	0.65 kHz
	Mean red channel background signal, B <sub>R</sub>	0.42 kHz
	Donor fluorophore quantum yield, $\Phi_{F,D}$	0.69
	Acceptor fluorophore quantum yield, $\Phi_{F,A}$	0.42

## **Movie S1**

The supplementary movie represents  $\sim\!65$  ns of the total simulation time. It shows various aspects of the p27 dynamics on different timescales, including transient formation and loss of LH helical secondary structure, bunching and elongation of the post-KID region near the helix, and global compaction and elongation.

## **Supplementary References**

- [1] Tsytlonok M, Sanabria H, Wang Y, Felekyan S, Hemmen K, Phillips AH, et al., Dynamic anticipation by Cdk2/Cyclin A-bound p27 mediates signal integration in cell cycle regulation, Nature communications. 10 (2019) 1676.
- [2] Hellenkamp B, Schmid S, Doroshenko O, Opanasyuk O, Kuhnemuth R, Rezaei Adariani S, et al., Precision and accuracy of single-molecule FRET measurements-a multi-laboratory benchmark study, Nat Methods. 15 (2018) 669-676.